A seismic tomography, gravity, and flexure study of the crust and upper mantle structure across the Hawaiian Ridge, Part 2 Ka‘ena

R. A. Dunn[1,*], A. B. Watts[2], C. Xu[2,3], and D. J. Shillington[4]

[1]Department of Earth Sciences, School of Ocean and Earth Science and Technology, University of Hawaii at Manoa, Honolulu, HI, USA.
[2]Department of Earth Sciences, University of Oxford, Oxford, UK.
[3]Key Lab of Submarine Geosciences and Prospecting Techniques, Ministry of Education, and College of Marine Geosciences, Ocean University of China, Qingdao, China.
[4]School of Earth and Sustainability, Northern Arizona University, Flagstaff, AZ, USA.

[*]Corresponding author. ORCID: orcid.org/0000-0003-1434-5512

Key words: Hawaiian Ridge; Volcano structure; Plate loading; Lithospheric flexure; Seismic tomography; Marine gravity

Key points:

The Hawaiian Ridge at Ka’ena consists of volcanic edifices ~7 km thick, sitting on Pacific oceanic crust ~6 km thick.

Seismic and gravity data reveal an inner volcanic core draped by layers of lava flows and volcanic debris.

Broad lithospheric flexure (peak deflection ~3.5 km) suggests a flexural rigidity of the 90 Myr old lithosphere equivalent to T_e = ~25.6 km.

Abstract. The Hawaiian Ridge, a classic intraplate volcanic chain in the Central Pacific Ocean, has long attracted researchers due to its origin, eruption patterns, and impact on lithospheric deformation. Thought to arise from pressure-release melting within a mantle plume, its mass-induced deformation of Earth's surface depends on load distribution and lithospheric properties, including elastic thickness (T_e). To investigate these features, a marine geophysical campaign was carried out across the Hawaiian Ridge in 2018. Westward of the island of Oʻahu, a seismic tomographic image, validated by gravity data, reveals a large mass of volcanic material emplaced on the oceanic crust, flanked by an apron of volcaniclastic material filling the moat created by plate flexure. The ridge adds ~7 km of material to pre-existing ~6-km-thick oceanic crust. A high-velocity and high-density core resides within the volcanic edifice, draped by alternating lava flows and mass wasting material. Beneath the edifice, upper mantle velocities are slightly higher than that of the surrounding mantle, and there is no evidence of extensive magmatic underplating of the crust. There is ~3.5 km of downward deflection of the sediment-crust and crust-mantle boundaries due to flexure in response to the volcanic load. At Kaʻena Ridge, the volcanic edifice's height and cross-sectional area are no more than half as large as those determined at Hawaiʻi Island. Together, these studies confirm that volcanic loads to the west of Hawai'i are largely compensated by flexure. Comparisons to the Emperor Seamount Chain confirm the Hawaiian Ridge's relatively stronger lithospheric rigidity.

Plain Language Summary

The Hawaiian Ridge, a seafloor volcanic chain in the Pacific, has long fascinated scientists for its origin, eruptions, and impact on Earth's surface layers. It is believed to form from melted rock originating in the Earth's mantle. As lava builds up each volcanic edifice, it presses down on the Earth's surface, deforming it by a few kilometers vertically, with the degree of deformation depending on its weight and the properties of the Earth's outer layers. Our geophysical study has imaged the interior of the volcanic ridge and the underlying crust and mantle. The volcano contains an interior core of highly crystalline rocks draped by volcanic material, and contributes to a broad lithospheric flexural response of up to ~3.5 km, vertically. This study sheds light on volcano formation, load-induced lithospheric flexure, and their implications for understanding Earth's subsurface processes.

1. Introduction

Located in the Central Pacific Ocean, the Hawaiian Ridge is one of the most prominent examples of an intraplate volcanic chain on the surface of the Earth. Long believed to have been created by pressure-release melting within a rising mantle plume (e.g., Morgan, 1971; Wilson, 1963), the large mass of the Hawaiian Ridge has inspired many studies on the manner in which the Earth's surface and upper layers yield to long-term surface loads. As each successive volcano in the Hawaiian Ridge grows, its large mass deforms the Earth's surface, resulting in a deflection or flexure of the lithosphere (e.g., Gunn, 1943; Walcott, 1970; Watts, 2001; Watts & Cochran, 1974; Watts & ten Brink, 1989; Wessel, 1993), the study of which can provide significant information about the stress state, flexural rigidity and rheological properties of the oceanic lithosphere (Calmant, 1987; Watts & Cochran, 1974). The degree of deformation is expected to be controlled, in part, by the mass distribution of the load, and the effective elastic thickness (T_e) of the lithosphere.

Along the Hawaiian Ridge, the volcanic load distribution is not well understood. Seismic, gravity, petrologic, and other studies reveal that the ridge is composed of a series of massive often-overlapping shield volcanoes, some of which appear to have cumulate cores. Early gravity and seismic experiments found evidence for high-density or high-wave-speed bodies within the islands of Oʻahu and Hawaiʻi (e.g., Adams & Furumoto, 1965; Strange et al., 1965a; 1965b; Woollard, 1951; Zucca et al., 1982) that were suggested to be each the result of up to a few million years of accumulated mafic and ultramafic intrusive materials. More recently, an updated residual gravity anomaly map of the Hawaiian Ridge (Flinders et al., 2013) and 2-D and 3-D seismic tomographic imaging studies across the island of Hawaiʻi and its submarine flanks clearly show that the summits and upper rift zones of volcanoes are characterized by high-density and high-velocity materials (Lin et al., 2014; MacGregor et al., 2023; Park et al., 2007; Park et al., 2009). Cumulate core features have been found by previous studies at other seamounts as well, e.g., Jimmu guyot on the Emperor Seamounts (Watts et al., 2021; Xu et al., 2022), Jasper seamount (Hammer et al., 1994), Louisville guyot (Contreras-Reyes et al., 2010), Great Meteor seamount (Weigel & Grevemeyer, 1999) and La Reunion Island (Gallart et al., 1999). Furthermore, not all of the added material may have been emplaced above the oceanic crust. A seismic study by Watts et al. (1985) along the Hawaiian Ridge indicated the possibility that magmatic material had been underplated to the bottom of the oceanic crust, setting off years of investigation into the degree of underplating beneath seamounts around the world (e.g., Ali et al., 2003; Caress et al., 1995; Dañobeitia and Canales, 2000 ; Leahy et al., 2010; Weigel and Grevemeyer, 1999). Where present, it may have important implications for load and buoyancy forces that control flexure (e.g., Wolfe et al., 1994).

The degree of deformation of the lithosphere is difficult to ascertain directly due to sediment cover and the presence of the ridge itself. However, flexure is readily apparent in a regional free-air gravity anomaly map (Figure 1), which reveals the Hawiian Moat, the seafloor depression around the Ridge that is partially filled by sediment. Previous seismic reflection and refraction experiments presented a variable but obvious increase in depth of the sediment-crust and crust-mantle boundary, or Moho, from the arch, beneath the moat, to the ridge near the islands of Maui, Oʻahu and Hawaiʻi (e.g., Furumoto & Woollard, 1965; Park et al., 2007; Shor & Pollard, 1964; Zucca et al., 1982). In comparison to the Emperor Seamount Chain, where plate age at the time of loading is relatively younger, studies of lithospheric flexure have suggested the lithosphere underlying the Hawaiian Ridge has a relatively stronger flexural rigidity and hence larger T_e values (Watts, 1978; Watts & Ribe, 1984; Watts et al., 2013). The first seismic experiment directly aimed at investigating flexure along the Hawaiian Ridge, was carried out in 1982 aboard the R/V *Robert D. Conrad* and the R/V *Kana Keoki* (Watts et al., 1985). The findings of the experiment revealed that the depth below sea level to the Moho, the boundary between the crust and the mantle, increased from approximately 11 km below sea level beneath the arch to over 14 km below sea level beneath the ridge.

The uncertainties in load distribution and corresponding degree and extent of flexure, leave models of mantle properties without substantial constraints. To address this issue, in 2018 we conducted a marine geophysical experiment across the Hawaiian Ridge, as part of a broader study of the seismic structure of the Hawaiian-Emperor Seamount Chain (Boston et al., 2019; Cilli et al., 2023; MacGregor et al., 2023; Watts et al., 2021; Xu et al., 2022). The experiment consisted of two ocean bottom seismograph (OBS) lines for tomographic imaging (Lines 01 and 02 in Figure 1) and seven MCS lines, along with corresponding gravity and multibeam bathymetry data collection (e.g., Watts et al, 2020). In this paper, we report results from the seismic and gravity profile located to the western side of the island of Oʻahu (Line 02; Figures 1 and 2) across the Kaʻena ridge. This paper is a companion paper to MacGregor et al., (2023), which analyzed data collected along Line 01 located across the western flank of the island of Hawaii. Our findings reveal that the Kaʻena Ridge consists of a volcanic edifice of ~7 km thick, which overlays pre-existing Pacific oceanic crust with a thickness of ~6 km. The edifice has a high-velocity and high-density core, consistent with intrusive mafic and/or ultramafic rock overlain by volcanic units and debris flows. The volcanic load produces a broad flexural response of the Pacific lithosphere with a peak vertical deflection of ~3.5 km. The results obtained from seismic tomography and gravity modeling are utilized to estimate the elastic thickness of the Pacific oceanic lithosphere and are compared to the results for Line 01 (MacGregor et al., 2023), as well as to results of comparable studies located along the Emperor Seamounts (Watts et al., 2022; Xu et al., 2022).

2. Study area

The oceanic crust that underlies the study area was formed at the Pacific-Farallon Ridge during the Cretaceous Period, approximately 90 Ma, at an estimated spreading rate of roughly 80 km/Myr (Seton et al., 2020). Prior seismic studies have found that the crust has a thickness of ~6-6.5 km and a seismic profile typical of oceanic crust formed along fast spreading ridges (e.g., Ohira et al., 2018; Watts et al., 1985). North of the islands, Ohira et al. (2018) found 9% mantle *P*-wave anisotropy, presumably due to the alignment of olivine crystallographic a-axes during seafloor spreading (Hess, 1964). Our seismic line is oriented ~58˚ from the paleo-spreading direction, or roughly intermediate between the seismically fast and slow directions.

The seismic line intersects the Hawaiian Ridge at Kaʻena Ridge (Figures 1 and 2), a submarine topographic high extending approximately 100 km northwest from Oʻahu towards Kauai. Kaʻena Ridge, with its expansive spatial area and shallowly-submerged summits, has frequently been proposed as an independent center of volcanism separate from the two volcanoes that comprise the island of Oʻahu: Waiʻanae and Koʻolau (e.g., Moore et al., 1989). Sinton et al. (2014), who analyzed seafloor samples, bathymetry, and gravity data, present compelling evidence that Kaʻena Ridge formed as a distinct shield volcano with a significant shield building phase occurring approximately 3.5 - 5 Ma, predating the major shield building stage of Waiʻanae volcano by up to 1 My. The upper sections of the volcanic structure are expected to have emerged above the water surface, reaching heights of approximately 1000 m, before subsiding due to the flexural response of the lithosphere caused by the added weight of Waiʻanae and Koʻolau volcanoes to the southeast.

Cutting across the region is the Molokai Fracture Zone (Figure 1), which is composed of several interacting tectonic strands oriented in an ENE-WSW direction, corresponding to the presumed Cretaceous spreading direction (e.g., Normark et al., 1989). Where observable, the abyssal hill fabric, which forms during the rifting process at the spreading ridge (e.g., Buck & Poliakov, 1998), is perpendicular to the lineament trend. The seafloor to the north of the fracture zone is younger compared to the southern side (e.g., Seton et al., 2020). As the fracture zone nears the Hawaiian Ridge, its morphological features gradually fade as the strands become buried beneath the sediments of the Hawaiian Moat and the Ridge itself, but it is largely observable in the gravity field (Figure 1). Along the southern side of Kaʻena, the seismic line intersects two splays of the fracture zone, near seismic stations 209 and 217 (Figure 2a).

The seismic line intersects submarine landslides on both sides of the Kaʻena Ridge. On the northern flank, there is a significant landslide deposit known as the Kaʻena Slide (Figure 2b), which is believed to have formed predominantly from a debris avalanche that scattered blocks of material into the Hawaiian Moat, covering a distance of over 90 km (Moore et al., 1989). The composition of samples collected from the deposit aligns with origins from Kaʻena Volcano, indicating that the slide occurred during the later stages of the volcanic edifice's growth (Sinton et al., 2014). Based on the difference in elevation between the deposit and the surrounding seafloor, the upper portion, characterized by a more coherent slump feature, generally has a thickness of less than 1 km, while the lower portion is typically less than a few hundred meters thick. The spatial extent of the slide depicted in Figure 2b is derived from Sinton et al. (2014). However, it is possible that this slide or a previous one extends further into the moat, as there seems to be an additional ~100 m of infilling material to the NNE of the defined area.

On the southern flank of the ridge is the Waiʻanae Slump, an extensive submarine landslide (Coombs et al., 2004; Hussong et al., 1987; Moore et al., 1989). Detailed seafloor mapping, on-bottom visual observations, and petrologic analyses, indicate that the landslide occurred as a complex series of slumps and smaller debris avalanches (Coombs et al., 2004; Sinton et al., 2014). The thickness of the slump has been estimated to be around 1-2 km (Presley et al., 1997). To the southwest of the Waiʻanae Slump lies a substantial debris field that stretches across the abyssal seafloor, covering an area of at least 2700 km^3 (Figure 2b). Coombs et al. (2004) suggested that this debris field likely formed approximately concurrently with the activity of the Wai‘anae Slump. When comparing the depth of the deposit to the surrounding seafloor, its thickness along the seismic line measures up to 500 m. However, this estimation is complicated by the overlapping volcanic features of the Southwest O‘ahu Volcanic Field.

The Southwest O‘ahu Volcanic Field (Figure 2b) was mapped in the late 1980s by GLORIA sidescan imagery (e.g., Holcomb & Robinson, 2004) and its volcanics were later investigated by Takahashi et al. (2001). It was found to be composed of numerous cones and thin lava flows. On the basis of seafloor samples and relationships, Coombs et al. (2004) argued that the volcanic field post-dates the debris field. Age estimates for the lava flows span 1.5-3 Ma (Coombs et al., 2004; Noguchi & Nakagawa, 2003), postdating Ka‘ena's main shield building stage.

The northern end of the seismic line intersects portions of the North Arch volcanic field (Figure 2a), which consists of nearly 25,000 km^2 of ~0.5-1.15 Ma age lava flows (Clague et al., 1990). The seismic line crosses the youngest of the flows (on the basis of backscatter imagery), where the flows are thought to be thin, a few tens of meters thick at most, with only isolated regions of thicker material near vents (Normark et al., 1989). Only a thin layer of sediment (~1 m thick) is expected to cover these flows.

3. Seismic experiment, data, and methods

The seismic data were collected in 2018 using the R/V *Marcus G. Langseth* (cruise MGL1806) and its 36-element 6,600-cubic-inch airgun array. The experiment consisted of two ocean bottom seismograph (OBS) tomography lines and seven multi-channel seismic (MCS) lines (Figure 1). This study analyzes data collected along the western OBS line, a ~550-km-long line centered on the Ka‘ena Ridge (Figure 2). For 2-D refraction tomography, 35 OBS were deployed along the line with an average spacing of ~15 km. Each OBS contained a hydrophone and a 3-component geophone and recorded at a sampling rate of 200 Hz. The line was shot twice, once with airgun pulses triggered every 390 m, which will be referred to as the "OBS shots", and once with pulses located every 63 m, which will be referred to as the "MCS shots", since that line was primarily for MCS analysis. Seismic waves recorded by the OBS from both sets of shots are included in the analysis presented here. The MCS shots provide dense coverage at short ranges, and a more limited amount of long-range data that varied by station. A collection of records for each station and the details on the OBS relocation, time base, and travel time picking approach is available in the online Supporting Information accompanying this paper.

A variety of seismic *P*-wave phases were identified and used in the analysis. The presence and timing of a particular phase is largely dependent on a station's distance from the Hawaiian Ridge. Most of the off-ridge stations recorded data to 300-350 km range, and *P* waves undershoot the Ka‘ena Ridge at crustal and mantle depths. Even seismic phases recorded from the MCS shot line can be identified at distances >200 km for some instruments, since waterborne shot noise is blocked by the ridge, facilitating the observation of long-range arrivals even if short-range data is obscured by prior shot noise. The record in Figure 3 is typical for stations located away from the ridge, showing a large delay in arrivals for shots located across the top of Ka‘ena that is presumably due to an increase in total crustal thickness. Figures 4 and 5 display sets of records that emphasize the crustal and mantle phases dominating at shorter ranges in the moat and across the Ka‘ena Ridge, respectively. Figure 6 shows a plot of the travel times for all stations and identified seismic phases, color-coded by type. There is very good data coverage and correspondence of phases from station to station, meaning that shot-station pairs align well with corresponding pairs in reversed positions. Figure 7 shows *Pn* travel times plotted with a reduced time axis to illustrate the change in mantle wave speed along the seismic line. The next two sections discuss the seismic phases in more detail.

3.1 Stations located to the north and south of the Hawaiian Ridge

Stations located away from the Ka‘ena Ridge (Figures 3 and 4) exhibit typical seismic phases for oceanic crust. The dominant seismic phases are *P*-wave refractions, which, in line with standard practice, are interpreted as occurring in the sediment layer (*P1*), upper oceanic crust (*P2*), lower oceanic crust (*P3*), and mantle (*Pn*). Additionally, reflections or triplications interpreted to occur at the top of the oceanic crust (*P2P*) and crust-mantle interface, or Moho, (*PmP*) are present. *P2P* is easily recognizable across the moat areas, where the records indicate the sediment is thickest (e.g., Figure 4g), compared to outside the moat areas (e.g., Figure 4h), where sediment appears to be thinner, and identifying a *P2P* arrival can be more challenging.

The apparent velocities of phases in the record sections indicate a relatively simple oceanic crustal structure with low-velocity upper layers, a ~7 km/s lower crust, and an upper mantle with a wave speed of about 8 km/s on average. The northern side of the seismic line suggests laterally homogeneous structures, while the area to the south, especially beneath the Southwest Oʻahu Volcanic Field and the southernmost strand of the Molokaʻi Fracture Zone (near stations 208 and 209), wave arrival times and amplitude variations suggest that the crustal structure is somewhat anomalous. Some records show clear *PmP* arrivals over large ranges (e.g., station 215 for shots to the south; Figure 4), while others show more limited *PmP* arrivals, but robust *Pn* arrivals (e.g., stations 208 and 231 for shots to the north; Figures 3 and 4). This suggests that the crust-mantle boundary is more transitional in some locations on the scale of a seismic wavelength, rather than a sharp contact. The strong *Pn* arrivals indicate a positive velocity gradient in the upper mantle. *PmP* was typically picked at ranges <60-80 km to avoid confusions with other waveform energy in the records.

There is some evidence for a two-step Moho, primarily associated with the southern part of the line where waves travel beneath the Southwest Oʻahu Volcanic Field. For instance, station 208 (Figure 3, inset) demonstrates evidence of a slightly slower *Pn* precursor phase to the primary *Pn* phase. There is also evidence for a few sparse sub-Moho reflection events (e.g., Figures 4e, 4f, and 4i), indicating the possible existence of individual frozen melt sills. But these do not occur with enough frequency to detectably reduce upper mantle velocities in a general sense. Overall, there is no evidence for a broad low-velocity crust-mantle mixed layer that underplates the oceanic crust, as has been suggested by past active-source (e.g., ten Brink & Brocher, 1987; Watts et al, 1985) or passive-source (receiver function) seismic studies (e.g., Leahy et al., 2010).

Figure 7 shows *Pn* travel times using a reduced time axis to align the arrival times. The reduction velocity that best aligns the refracted arrivals can be taken as an approximation of the velocity for those ray paths, whereas the overall trends in the arrivals suggest broad structural changes. The broad trend is a general delay for ray paths approaching the ridge, probably due to the increase in sediment in the moats followed by increased crustal thickness at the ridge. However, *Pn* arrivals do not align for any single reduction velocity (8 km/s in Figure 7a), indicating lateral variations in mantle structure. Away from the ridge, the apparent velocity of the travel times is close to 8 km/s (Figure 7a,c), but varies locally from values of ~7.8 km/s to 8.2 km/s. The sub-ridge area is discussed in Section 3.2.

3.2 Stations located on the volcanic edifice and its flanks

As stations approach the Kaʻena Ridge, phase identification becomes more difficult due to travel time delays and scattering caused by edifice topography and lateral velocity gradients. The slopes of travel time curves are unreliable indicators of the seismic phase. Station-shot pairs were examined in reverse configurations to ensure consistency. Several seismic phases, including *P1*, *P2*, *P3*, *P2P*, *PmP*, and *Pn*, were observed, and an additional phase, *Pv*, was identified as waves travelling through the volcanic edifice above the oceanic crust. Distinguishing between *P1* and *Pv* could be challenging in some places, but it does not affect imaging since these phases are treated similarly in the tomographic method (likewise for the *P2* and *P3* phase pair).

For stations located atop the ridge (Figure 5), the records exhibit a clear asymmetry in *Pv* arrivals across a midpoint between stations 219 and 220. The apparent velocities for shots moving away from that midpoint are slower than expected for intrusive rocks, indicating layers of lava flows possibly mixed with debris from submarine landslides that occurred during the shield building stage. For ray paths crossing the midpoint between stations 219 and 220, the *Pv* phase shows a rapid change in slope with increasing range, indicating the presence of a central high-velocity body within the edifice of the volcano. In Figures 5 and S4b-d, *P2P*, *P3*, and *PmP* arrivals all indicate a deepening of the oceanic crust and Moho beneath the Kaʻena Ridge. Some possible sub-Moho reflection events are also observed (e.g., Figure 5f), suggesting the presence of frozen melt sills. Secondary phases in Figure 5e indicate step-changes in velocity structure within or at the base of the Waiʻanae Slump.

Pn data show progressive time delays toward the ridge, indicating thickening upper layers and a deepening Moho (Figure 7a). In addition, for stations located on one side of the ridge and shots on the other, the travel times of *Pn* waves that undershoot the edifice arrive much earlier than expected when assuming an 8 km/s mantle (Figure 7a). These data are best aligned with a reduction velocity of ~8.25 km/s (Figure 7b; green dots). To emphasize the sensitivity of the phase alignment with changes in reduction velocity, a reduction velocity of 7.8 km/s is also shown (Figure 7b; gray dots) and is strongly inconsistent with the data. On the other hand, 7.8 km/s provides a good fit to other *Pn* arrivals along the seismic line for rays that do not undershoot the ridge axis (Figure 7c). From these considerations, we expect that mantle velocities are variable and relatively high (8.2-8.3 km/s) beneath the ridge and lower elsewhere.

3.3 Seismic methods

Seismic imaging was carried out using an iterative tomographic technique that uses travel time data to compute seismic velocity structure (Dunn et al., 2005). This implementation is capable of handling both primary and secondary refracted and reflected phases. Internal reflectors are defined on their own grid for ray-tracing accuracy and velocities defined on the principal grid move vertically with changes in reflector position. The imaging procedure was carried out by first solving for upper crustal structure with a shallow reflector representing the top of the oceanic crust, and then solving for the full structure with a second reflector representing the top of the mantle (the tomographic technique allows for only one reflector at a time). In each case, a starting model was first determined and then 150 solutions were created by varying that starting model. A single final solution was then determined by taking the mean of the stack of solutions, the standard deviation of the stack provides a measure of the relative uncertainty of the image. More details on the methodology and uncertainties are provided in the Supporting Information file that accompanies this submission. The final tomographic image is shown in Figure 8.

4. Gravity data and processing

Gravity data were acquired throughout cruise MGL1806, including along each seismic reflection and refraction line. In this study, we analyze the gravity data collected along OBS seismic Line 02 (Figure 2), coincident with the present seismic tomography analysis.

Gravity data were acquired with an axially-constrained BGM-3 sensor mounted on a gyrostabilized platform. In June 2018, the sensor was replaced and the instrument recalibrated with a new pulse rate count to mGal conversion factor of 5.096606269 mGal/count and bias of 852,513.49 mGal using tie-in data between the BGM-3 gravimeter and the Honolulu Alpha absolute gravity station. Tie-in data since June 2018 indicate that the new sensor system has performed well with a mistie at the start MGL1806 (some 80 days later) of -6.1 mGal, a mistie of +1.5 mGal at the end of the cruise and a drift rate of -0.155 mGal/day during the cruise (Watts et al., 2020).

Prior to correcting for latitude and the Eötvös effect, the 1 s converted count data were filtered with a 120 s Gaussian filter in order to remove accelerations due to ship motions, as recommended by the manufacturer (Bell Aerospace). While we found such a filter to be highly effective at removing swell "noise" (Watts et al., 2020), noise remained at high frequencies (short periods), albeit with significantly less power than swell "noise". We therefore applied an additional filtering step to the count data using a median filter (width = 1.0 km), which reduced the high frequency noise and, importantly, extended the overall decrease in power with increasing frequency seen in spectral data at low frequencies. The free-air anomaly was calculated from the cleaned gravity data.

5. Seismic structure

5.1 The Ka‘ena Ridge

The volcanic edifice consists of a relatively high V*p* inner "core", surrounded by a highly variable region of overall lower velocities (Figure 8). This structure is generally consistent with previous studies that have detected localized high-density, high velocity cores within other Hawaiian volcanoes (e.g., Adams & Furumoto, 1965; Strange et al., 1965a; 1965b; Woollard, 1951; Flinders et al., 2013). At Ka‘ena, the width of the core is ~30 km, and it stands ~5 km high. V*p* values reach a peak of ~7 km/s within the upper central part of the core. Overall, this feature is consistent with a mix of intrusive and extrusive material. Immediately to the south of this feature, there is a smaller, less-pronounced core-like structure. On the northern flank of the edifice, near surface velocities beneath the Ka‘ena slide are low (<3 km/s), and the interior of the flank is composed of large outward-dipping layers of alternating velocities. Likewise, the south flank of the edifice, which includes the Wai'anae Slump, exhibits low near-surface velocities followed by layers of alternating velocities within the interior. The small topographic depression that formed between the edifice and the Wai'anae Slump appears to be filled with low-velocity in-fill material. The maximum thickness of material added to the top of the oceanic crust is ~7 km and the width of the edifice is about 100 km at its base.

5.2 Oceanic Crust and Mantle

Away from the complexities of the Hawaiian Ridge, the crust has a typical V*p* profile for Pacific oceanic crust, with a thin sub-seafloor low-velocity layer (<4.5 km/s; seismic layer 1) characteristic of accumulated volcaniclastic and oceanic sediments, a thicker low-velocity layer (4-6.5 km/s; seismic layer 2), usually thought to be the upper oceanic crust and composed of dikes and lava flows, and a deeper high-velocity layer (~6.5-7 km/s; seismic layer 3), usually thought to be the lower oceanic crust and composed of intrusive gabbroic rocks (Figure 8) (e.g., Christeson et al., 2019). Using the distance between the two reflectors as a guide, the median crustal thickness is 6 km, a typical value for oceanic crust formed at faster spreading rates (e.g., Christeson et al., 2019). The crust is thicker to the south (~6.3 km) than to the north (~5.5 km) of the fracture zone. This asymmetry is similar to that found during a previous study of seismic structure in this region (ten Brink & Brocher, 1988). Note that the nature of the upper reflector is uncertain. While it appears to be the boundary between sediments and the oceanic crust, the velocity contrast between volcaniclastic sediments and 90 Ma seafloor may not be large, and it is possible that the reflector indicates a deeper feature, such as the seismic layer 2A/2B boundary.

The lower crust is fairly uniform beneath the northern part of the line, and more variable beneath the southern part of the line, perhaps due to modification via the Southwest O‘ahu Volcanic Field and the fracture zone splays that pass through this area (Figure 8). For example, a distinct low velocity zone is observed in the lower oceanic crust beneath the southern strand of the fracture zone (at -140 km of the profile) and a weaker one is observed beneath the northern strand (at -30 km of the profile). Given their association with the fracture zone, they may be due to crustal damage, increased porosity, and alteration (e.g., Roland et al., 2012).

Over wide areas along the seismic line (Figure 8; -250 to -180 km and 140 to 200 km), the lower crust, at a depth of 4-5 km bsf, has slightly lower velocity than material just above. This is corroborated by seismic records for these areas, which show the rapid loss of refracted *P3* wave energy with increasing ray turning depth, indicative of the presence of a negative vertical velocity gradient (Figures 4a and S1).

Approaching the Ka‘ena Ridge, the sediment layer thickens and the shallow seismic reflector deepens at a greater rate than the seafloor (Figure 8). This indicates increasing downward curvature of the top of the crust toward the edifice, presumably due to flexural loading of the plate. The overall deflection of the top of the oceanic crust beneath the edifice (with respect to its position at the ends of the seismic line) is ~3 km. The same measurement for the Moho yields a value of ~3.5 km. In the upper oceanic crust, the lowest V*p* values correspond with the location of maximum curvature, just outboard of the flanks of the edifice.

Beneath the edifice, the oceanic crust has anomalously high velocities at all levels (Figure 8). The low-velocity layer at the top of the crust is missing over a region roughly 75 km wide, replaced with velocities exceeding 6 km/s with a peak central value of ~7 km/s. In the lower crust, V*p* generally exceeds 7 km/s and rises to ~7.5 km/s just above the Moho reflector over a ~150 km wide area. The latter observation is difficult to verify with the travel time data alone. Given the possible trade-off of V*p* values with crustal thickness just above the Moho (a 1 km Moho depth change relates to a change in Vp of almost ~0.4 km/s above the Moho; Figure S6), we suggest caution when interpreting this.

Beneath the Hawaiian Ridge, a high V*p* region extends downward into the mantle, widening with depth. Here, mantle V*p* exceeds 8.25 km/s over a wide area beneath the edifice, as compared to ~7.75-8 km/s outside of this area. Note that in the study area, the seismogenic layer thickness is expected to be >40 km thick, on the basis of the depth limit of seismicity (e.g., McKenzie et al., 2005), and therefore the image is entirely contained within this layer. Overall, the mantle exhibits a small positive gradient with depth of ~0.01 km/s per km of depth. There is no evidence in the image nor in the data records themselves for a distinct sub-crustal low-velocity layer (with velocities between crust and mantle values) either located beneath the edifice (Watts et al., 1985) or underlying a broad area around the islands (Leahy et al., 2010).

6. Gravity anomalies

To verify the final seismic tomographic image, we computed the gravity effect of the seismically constrained crust and mantle structure assuming different empirical relationships between *P* wave velocity and density and compared it to the observed free-air gravity anomaly. Figure 9 shows the observed and calculated gravity anomalies along Line 02, the iso-velocity contours derived from Figure 8 and the density structure used in the gravity calculations. The calculated gravity is based on a layered structure in which the density contrast between layers is derived from the average *P* wave velocity above and below an individual iso-velocity contour. Figure 9a (black solid line) shows the sum of the gravity effect of all the layers, which was computed using a 3D Fast Fourier Transform modelling method for the seafloor bathymetry and a 2D line-integral method for each sub-seafloor layer and an empirical relationship between *P* wave velocity and density as defined by Nafe-Drake for 1.5 < V*p* < 5.5 km/s and Christensen and Mooney for V*p* >= 5.5 km/s (Brocher, 2005).

Figure 9a shows a close agreement between the calculated gravity effect of the seismically constrained crust and mantle structure in Figure 8 and the observed free-air gravity anomaly. The Root Mean Square (RMS) difference between observed and calculated gravity is 8.7 mGal, which is small when compared to the range of the observed free-air anomalies (~-75 to +225 mGal). The main discrepancies are in the region of the flexural moat northeast of Oʻahu where the calculated gravity effect is generally too low compared to the observed anomaly. The discrepancy correlates with a 50-km wide region of relatively low density in the uppermost part of the sub-crustal mantle and so we speculate that it is caused by a slightly denser mantle beneath the moat northeast of Oʻahu than beneath the moat to the southwest of the island. A more localized discrepancy occurs over the crest of the Kaʻena Ridge which we attribute to the three-dimensional structure of the high velocity core of the volcanic edifice.

The contributions of the individual sub-seafloor layers to the calculated gravity are shown in Figure S8 of Supporting Information. That figure, together with Figure 9a, shows the observed gravity high over the edifice is due to a combination of the gravity effect of seafloor bathymetry and the shallowing of the sub-seafloor 3-7 km/s iso-velocity contours, with the amplitude and wavelength of the high mainly controlled by the gravity effect of the 5.5-7 and 3-5 km/s iso-velocity contours respectively. Seismic and gravity data therefore reflect the origin of the volcanic edifice with its low velocity and density extrusive drape and its high velocity and density intrusive core. Flanking the high are lows that are mainly caused by the gravity effect of an increase in depth of the 5-7.5 km/s contours from the bulge region to beneath the edifice. We attribute this increase to crustal flexure in response to long-term (> 1 Myr) volcano loading. Competing with the gravity anomaly high and flanking lows associated with flexure is the mantle structure, and our seismic and gravity modelling are consistent with the existence of a relatively high *P* wave velocity and density mantle beneath the volcanic edifice and relatively low *P* wave velocity and density mantle beneath its flanking moats.

7. Discussion

7.1 Oceanic crustal and upper mantle structure

In the moat areas, sediment wave speeds are <3 km/s near the seafloor in places, and generally <5 km/s everywhere else (Figure 8). This is consistent with volcaniclastic sediments (e.g., Hammer et al., 1994; Weigel & Grevemeyer, 1999), overlain by a thin layer of mixed oceanic and volcanic sediment. There is no clear distinction between moat material and the material that makes up the flanks of the edifice, and these materials are probably greatly intermingled at the outer edges of the edifice (Figure 10).

At the intersections of the seismic line with strands of the fracture zone (Figures 8 and 10), the low velocity regions in the crust may be a consequence of fault damage and alteration (e.g., Roland et al., 2012). Between the two strands, the crust is somewhat thinner (~5.5 km), and thinner oceanic crust is often associated with fracture zone offsets (e.g., Detrick & Purdy, 1980; Detrick et al., 1993; Minshull et al., 1991; White et al., 1984), and is usually attributed to suppressed mantle melting near portions of the mid-ocean ridge where the fracture zone originated (e.g., Detrick et al., 1993; Stroup & Fox, 1981; White et al., 1984).

In the oceanic crust, away from the edifice and fracture zones, there are wide low-velocity regions at mid-crustal depth (Figure 8). We suggest that as the crust ages (e.g., Grevemeyer & Weigel, 1996), fractures and pore space that formed nearer to the mid-ocean ridge will seal from the top downward. This could result in relatively higher velocities overlying a region of relatively lower values where this process has not yet taken place. In the upper oceanic crust, the low V*p* values located at maximum downward plate curvature, just outboard of the flanks of the edifice, may be due to the formation of tensile cracks or larger fractures as a consequence of flexure, which would lower seismic wave speed (e.g., Berge et al., 1992).

Across the Hawaiian Ridge at Kaʻena, the edifice is about 7 km thick, and the oceanic crust plunges downward beneath the edifice, with a total deflection of ~3.5 km over a ~400-500-km-wide region (Figures 8 and 10). Beneath the edifice, the fate of the top of the oceanic crust is unknown. Presumably some combination of magmatic overprinting and compression of original pore space has led to higher velocities. Here, the upper reflector beneath the edifice is at a depth roughly consistent with the top of the oceanic crust (on the basis of its height above the Moho), unlike what was found near the Island of Hawai'i (MacGregor et al., 2023), where it appears that the dominant reflection marks the top of the lower oceanic crust and a reflection from the top of the oceanic crust is weak and intermittent. In the lower oceanic crust, near the Moho, elevated velocities, suggest magmatic overprinting, perhaps due to the crystallization of ultramafic minerals as melts enter the crust. Furthermore, below this region, we see elevated mantle velocities. This is well documented by the travel time data (e.g., Figure 7) and by the necessity for its presence to fit the gravity data (Figure 9). The gravity constraint is important, because it indicates a bulk mineralogical change, rather than a change in the orientation of anisotropic minerals in the mantle (i.e., an alignment of the fast axes that is more parallel to the seismic line). One could argue that the high wave speeds were inherited from processes in operation at the spreading center during crustal formation, but the feature's close association with the ridge suggests related processes rather than coincidence. The anomalous mantle wave speed suggests that melts beneath the ridge rose through the mantle and chemically interacted with the cooler lithosphere as they passed through, leaving behind a more ultramafic-rich material.

We find no evidence for significant underplating of melts beneath the Moho, as suggested by prior studies of Hawai'i (e.g., Leahy et al., 2010; Watts et al., 1985) and some other marine volcanoes (e.g., Gallart et al., 1999; Grevemeyer et al., 2001). We also rule out broad serpentinization of the upper mantle, as suggested by Park and Rye (2019), though there may be some minor local serpentinization such as indicated beneath the fracture zone. Instead, we find a simple Moho transition, with some variability in its character, as well as evidence for isolated sub-Moho frozen melt sills. Since the Ka'ena seismic line is not co-located with the previous study of Watts et al. (1985), the differences in interpretation (no underplating versus underplating) may simply indicate that underplating is variable along the ridge. However, reprocessing of the earlier seismic data has not found evidence for underplating (Lindwall, 1988; Cilli et al., 2023) and other recent studies of the Hawaiian-Emperor Seamount Chain have also not found evidence for underplating (McGregor et al., 2023; Watts et al., 2022; Xu et al., 2022).

We do find some local variations in V*p* that may be related to variable melt-rock reaction effects and/or inefficient melt extraction, along with evidence of a few sub-Moho reflectors. Ohira et al. (2018), using wide-angle seismic data from 750-km-long line located north of O‘ahu, also found evidence for several isolated sub-Moho frozen melt sills at depths ranging from 30-85 km, which they suggest formed during cooling of the plate. Imbedded within the high-velocity mantle region beneath the Ka‘ena Ridge is a smaller region of relatively lower velocities (~8 km/s) that lies directly beneath the ridge (Figure 8) and is associated with one of the possible sub-Moho melt lenses (Figure 5f). This small region could be a consequence of frozen mafic melts, associated with an incomplete separation of mafic and ultramafic material as the magmatic phase of the seamount waned. Other studies have also suggested incomplete melt extraction from the mantle, both in hot-spot effected areas (e.g., Gaherty & Dunn, 2007; Walther, 2003), and near mid-ocean ridges (e.g., Conley & Dunn, 2011; Lizarralde et al., 2004). Nevertheless, it would not represent a significant amount of melt as compared to the mass of the edifice or to previous suggestions of underplating.

7.2 Volcano structure

Although evidence suggests that Kaʻena Ridge formed as a separate shield volcano from that of Oʻahu's Waiʻanae volcano (Sinton et al., 2014), the location of its central vent and its structural association with Waiʻanae volcano and the Waiʻalu Ridge are uncertain. Many Hawaiian volcanoes are characterized by a central strong residual Bouguer gravity anomaly high (e.g., Flinders et al., 2013; Strange et al., 1965a) and shallow high-velocity bodies (e.g., Furumoto et al., 1965; Park et al., 2009), which are often ascribed to the location of the principle magmatic conduits through which the shield building stage of the volcano occurred, leaving behind dense, possibly olivine-rich, cumulates. On the basis of the gravity structure and other features of Kaʻena, Sinton et al. (2014) speculate that the center of Kaʻena Volcano lies buried beneath lava flows from Waiʻanae volcano at a position roughly centered just east of our seismic line (Figure 2b). The gravity anomaly in this area is modest, only ~10 mgal as compared to >50 mgal for Waiʻanae Volcano (Figure 2b). Sinton et al. (2014) suggest that the smaller gravity anomaly and overall morphology of Kaʻena are consistent with Kaʻena being a smaller volcano by volume, with more broadly disseminated volcanic activities. By this view, the portion of Kaʻena Ridge extending westward from the gravity anomaly, and Waiʻalu Ridge extending to the northwest, are consistent with being rift zones of Kaʻena Volcano.

The seismic line is located just along the western edge of the estimated center of volcanism of Kaʻena volcano (Figure 2b). Presumably then, the high-density and high-velocity core imaged here (Figure 10) is the western edge of the center of volcanism of Kaʻena volcano. Alternatively, the imaged core could be a slice of a more elongate feature that extends considerably along the Kaʻena Ridge, such as is expected for the core-like feature detected beneath the Hāna Ridge (MacGregor et al., 2023). The presence of the core suggests an edifice-level magma chamber or mush zone, which would have evolved considerably in size and elevation during volcano growth. The core properties are consistent with either intrusive gabbroic rocks, or a mixture of lavas, dikes, gabbro, and ultramafic cumulates (i.e., a mixture of both high and low density/velocity materials). The latter scenario seems more likely since magmatism would have built the core by intruding previously formed dikes and lavas. The smaller core-like feature to the south (Figure 10) may have its origin in a small southeasterly trending rift zone located beneath the slump and associated with a secondary center of volcanism of Kaʻena (Sinton et al., 2014).

Landslides of various types are ubiquitous features of the flanks of the Hawaiian Ridge. They appear to form by both gravitational sector collapse and by lateral forces resulting from magma injection into a volcano's rift zones (e.g., Moore et al, 1989). The shield stage of volcano growth may generate the most landslides, due to active lava emplacement and oversteepening of the volcano flanks (Coombs et al., 2004; Moore et al., 1989). The alternating layers of lower and higher seismic velocity (Figure 8) that characterize the flanks of Kaʻena Ridge may represent alternating lithologies (Figure 10), such as alternating layers of lava flows and debris avalanche material. This ‘layer-cake' structure may have implications for future landslides in that weaker layers may allow for large-scale sector collapse of the volcano, such as has already occurred at the Wai'anae Slump (Figure 2b). The slump is estimated to be ~1.5 km thick (Coombs et al., 2004), and may thus have given way along a zone of weakness indicated by a band of low velocities at that depth (Figure 8). Considering a trigger for the slump, we note that it overlies a splay of the Molokai Fracture Zone. The age asymmetry across the fracture zone indicates that the two halves of the plate have different thermomechanical properties and may have responded differently to the volcanic load. We speculate that as the Hawaiian Ridge grew across the fracture zone, there occurred enough differential flexure and vertical motion across it to trigger the slow collapse of the volcano flank.

7.3 Plate flexure

The tomographic model can be used together with bathymetry and gravity data to constrain the flexure caused by the volcanic load of the Hawaiian Ridge and the elastic parameters associated with this flexure. The load was derived from a regional GEBCO bathymetric grid, corrected for the effects of thermal age, assuming a cooling plate model (Parsons & Sclater, 1977) and the Müller et al. (1997) age grid, and for formation of the Hawaiian swell (e.g., Wessel, 2016), assuming it to be derived from a 500-km-wide median filter of the GEBCO bathymetric grid. We compared the average depth to the top of oceanic crust and the Moho derived from the tomographic model (red curves in Figure 8) to predictions based on a simple three-dimensional elastic plate (flexure) model. The 'best fit' parameters for the model were estimated from the RMS difference between the observed seismically constrained surfaces of top of oceanic crust and Moho and the calculated surfaces for a range of densities for the material infilling the flexure (ρ_{infill}) of 2100 to 2800 kg/m^3 and T_e of 0-60 km, assuming a load density (based on the *P* wave velocity structure of the volcanic edifice) of 2737 kg/m^3. The results are summarized in Figure S9 of Supporting Information which show a best fit parameter pair of ρ_{infill} = 2450 kg/m^3 and T_e = 25.6 km for the top of oceanic crust and ρ_{infill} = 2450 kg/m^3 and a slightly lower T_e = 23.1 km and the same ρ_{infill} = 2450 kg/m^3 for the Moho. The minimum RMS values for the two surfaces are 167.3 m and 325.9 m, respectively, indicating that the best overall fit (by a factor of 2) is for the top of oceanic crust. Changing the load density within bounds determined by the seismic constraints on the top of oceanic crust has little effect on the results: decreasing the load density to 2637 kg/m^3, for example, results in a best fit T_e, average ρ_{infill} and RMS of 23.1 km, 2500 kg/m^3 and 166.2 m respectively, while increasing the load density to 2867 kg/m^3 results in a best fit of 25.6 km, 2400 kg/m^3 and 164.1 m respectively.

The T_e results here are in general accord with the results of Cilli et al. (2023) using reprocessed R/V *Robert D. Conrad* and the R/V *Kana Keoki* multichannel seismic reflection profile data. They used a similar range of load densities and derived a T_e in the range 25.7 to 27.7 km, slightly higher than the values derived here. However, the *Conrad* and *Kana Keoki* profiles do not cross the Ka'ena Ridge, intersecting instead the Hawaiian Ridge at the deep channel that separates Kauai and O'ahu and the insular shelf between O'ahu and Moloka'i. In addition, a somewhat higher infill density was obtained (2701 kg/m^3) and perhaps, most significantly, the lowest RMS obtained for the top of the oceanic crust was 305.5 m, which is nearly a factor of 2 higher than that derived here.

The best-fit flexure model based on a load density to 2737 kg/m^3 and a pre-existing oceanic crustal thickness of 6.05 km (the mean difference between the depth to the two reflector surfaces in Figure 8) is shown by the light blue shading in Figure 9b. There is an excellent agreement between the seismically constrained surfaces of the top of oceanic crust and Moho and the calculated flexure. The fit between the observed and calculated free-air gravity anomaly (Figure 9a) is not, however, as close. We attribute the misfit to our assumptions that the only loads that act on the plate are surface loads as defined by the present-day bathymetry, and that the material infilling the flexure is of uniform density. For example, the bathymetry is not the only contributor to the positive part of the observed gravity anomaly. There is therefore likely to be a significant contribution to the gravity anomaly of sub-surface loads, especially those associated with the 5, 6 and 6.5 km/s iso-velocity contours. The effect of a non-uniform infill density is more difficult to assess. The flexure model in Figure 9b assumes an average ρ_{infill} = 2450 kg/m^3, but it is likely that ρ_{infill} immediately beneath the loads is higher and of the order of the load density and lower in the flanking flexural moats.

7.4 Comparison of Lines 01 and 02

In this study, we investigate the relationship between the Ka‘ena Ridge’s volcanic load distribution, lithospheric deformation, and elastic properties. The results for this geophysical line (Line 02) can be directly compared to those presented in our companion study (MacGregor et al., 2023) located to the west of Hawai’i (Line 01). The two studies examine plate flexure for situations in which the underlying plate age is similar, but the load size and structure are much different.

At Ka‘ena, the volcanic edifice's height and cross-sectional area are approximately half as large as those at Hawai‘i (Table 1). The presence of a large, high-density, and high-velocity core suggests that the seismic line intersects a significant portion of the volcano’s center of volcanism. The core’s properties are consistent with intrusive gabbroic rocks or a mixture of dense mafic and ultramafic materials, indicating the previous existence of an edifice-level magma chamber or mush zone. The proportion of intrusive to extrusive rocks is estimated at approximately 7% (excluding materials that may have entered the moat). In contrast, the western flank of the island of Hawaii lacks such a feature and appears to consist primarily of layer upon layer of extrusive rocks. The relatively smaller cross-section of the Hāna Ridge may comprise as much as ~20% dense intrusive material.

At Ka‘ena, the amount of deflection is about half that measured westward of the island of Hawai‘i (MacGregor et al., 2023). Despite the large difference in load size and flexure between the two locations, the calculated T_e values are similar (25.6 for Ka‘ena versus 26.7 westward of the island of Hawaii). These results are supported by Cilli et al. (2023), who used reprocessed legacy MCS data as a basis for additional flexural modelling near O‘ahu (T_e of 26.7), but largely eastward of the Ka‘ena seismic line. Together, these studies confirm that volcanic loads to the west of Hawai’i are largely compensated by flexure. However, as discussed in MacGregor et al.

(2023), previous studies suggest on-going subsidence and a higher T_e value beneath of the eastern flank of Hawai'i Island, suggesting that isostatic compensation may not yet be complete at the youngest end of the ridge.

Magmatic underplating beneath the oceanic crust has been suggested for several intraplate volcanic settings and affects loading and mass flux calculations. All else being equal, underplating would be expected to lower the amplitude of the gravity anomaly over the crest of the edifice and provide a positive buoyancy force that would make the plate appear more rigid than it actually is. One hypothesis put forward to explain variations in the style of magmatic emplacement at intraplate volcanoes hinges on the age of the lithosphere at the time of volcano formation. In this model, shallow intrusion into the oceanic crust and overlying edifice is favored for seamounts growing on young lithosphere, while magmatic underplating is favored for seamounts growing on old lithosphere (Contreras-Reyes et al., 2010). However, the recent seismic, gravity, and plate flexure studies conducted along the Hawaiian-Emperor Seamount Chain (including this study, MacGregor et al., 2023, Watts et al., 2021, and Xu et al., 2022) collectively provide clear evidence for shallow magmatic emplacement and contradict the notion of significant magmatic underplating for ages at the time of loading of ~57 Ma (Emperor Seamounts) and ~90 Ma (Hawaiian Ridge). Additionally, reprocessing of the legacy data of Watts et al. (1985) did not find evidence for underplating (Lindwall, 1988; Cilli et al., 2023). These findings invalidate a simple age-related hypothesis.

The recent seismic studies found only scant evidence for a mantle conduit that might be ascribed to a narrow zone where melts passed upwards towards a volcano along the ridge. Beneath the Ka'ena line we find a broad zone of high velocities that may be due to melt-rock reactions, and an inner region near the Moho of lower velocities wherein melts may have frozen before they could separate from the mantle. A similar structure may be present beneath Jimmu Guyot (Xu et al., 2022), while Watts et al. (2021), using a ridge parallel seismic line, found variations in mantle structure that are difficult to reconcile with any simple model of mantle conduits feeding the cores of ridge volcanoes. In these studies, at mantle levels the width of the minimum resolvable feature may be 20 km or more and perhaps regions of melt passage are too isolated or too narrow to significantly influence the seismic wavefield and cannot be imaged using these experiment geometries.

8. Conclusions

Using wide-angle seismic refraction and reflection data collected along a 550-km-long line that intersects the Hawaiian Ridge at Kaʻena volcano, we imaged the structure of the edifice and the underlying Pacific oceanic crust and upper mantle using *P* wave tomography. By modeling the density structure and gravity data and the degree of plate flexure, as determined by the seismic results, we investigated the relationship between the ridge's volcanic load distribution, lithospheric deformation, and elastic properties and compare the results to other studies located along the Hawaiian-Emperor Ridge. Our findings shed light on several key aspects of the Ridge's geological and geophysical characteristics.

Volcanic Construction and Load Distribution. Our seismic imaging and gravity data collectively provide evidence for a complex internal structure within the Hawaiian Ridge at Kaʻena Ridge, characterized by a high velocity, high density, core overlain by volcanic layers and debris flows. The presence of a cumulate core indicates that shallow intrusive processes shape the Ridge's volcanic evolution. The presence of this core is consistent with several other studies of Hawaiian volcanoes that have detected the presence of such features and ascribed them to central conduits of magmatic activity. Despite this interpretation, no corresponding features have been detected in the mantle. In addition, no wide-spread crustal underplating of magmatic material was detected here or beneath Hawaii island, but some scattered upper mantle intrusions are indicated by the seismic data. Shallow layer-cake structures beneath the flanks of Kaʻena Ridge may indicate zones of weakness that promote flank collapse.

Lithospheric Flexure. Lithospheric deformation is prominently expressed through the Hawaiian Moat and sub-ridge depression of the seismically determined sediment-crust and crust-mantle boundaries. The added load is up to ~7 km in height, and the flexural response is broad with a resultant peak vertical deflection of ~3.5 km, suggesting a flexural rigidity of the lithosphere which is ~90 Myr old, equivalent to T_e = ~25.6 km. This is similar to other recent estimates along the Hawaiian Ridge, despite the large differences in load size for these different studies. Comparisons to the Emperor Seamount Chain confirm the Hawaiian Ridge's relatively stronger lithospheric rigidity, emphasizing the significance of lithospheric age at the time of loading to the load-induced flexural response.

Acknowledgements. Seismic data used in this research were provided by instruments from the Ocean Bottom Seismic Instrument Center (OBSIC, 2022), which is funded by the National Science Foundation. MATLAB® (The Mathworks, 2021) and the Generic Mapping Tools (Wessel et al., 2019) were used to create figures. We are grateful to the captain, crew, science party, and the Party Watch, of the R/V Langseth leg MGL1806. This work was funded by NSF grant OCE-1737243 to R. A. Dunn and OCE-1737245 to D. J. Shillington and A. B. Watts.

Open Research. Cruise-related data (cruise identifier MGL1806) are stored at the Rolling Deck to Repository archive (R^2R, 2023). OBSIC data are archived at the EarthScope Consortium facilities (HI-Emperor, 2019; SAGE, 2023). The seismic models for Lines 01 and 02 are archived at Dunn et al. (2024) and Dunn (2024), respectively.

References

Adams, W. M., & Furumoto, A. S. (1965). A seismic refraction study of the Koolau volcanic plug. Pacific Science, 19(3): 296-305. http://hdl.handle.net/10125/10747

Berge, P.A., Fryer, G.J., Wilkens, R.H., (1992). Velocity–porosity relationships in the upper oceanic crust: theoretical considerations. Journal of Geophysical Research: Solid Earth, 97 (B11), 15239–15254.

Boston, B., Shillington, D. J., Dunn, R. A., Watts, A. B., Grevemeyer, I., Gomez de la Pena, L., et al. (2019). The crustal and upper mantle structure of the Hawaiian-Emperor Seamount Chain from marine seismic data. American Geophysical Union, Fall Meeting 2019, abstract #T41B-06.

Brocher, T. M. (2005). Empirical relations between elastic wavespeeds and density in the Earth's crust. Bulletin of the seismological Society of America, 95(6), 2081-2092. https://doi.org/10.1785/0120050077

Buck, W. R., & Poliakov, A. N. (1998). Abyssal hills formed by stretching oceanic lithosphere. Nature, 392(6673), 272-275. https://doi.org/10.1038/32636

Calmant, S. (1987). The elastic thickness of the lithosphere in the Pacific Ocean. Earth and Planetary Science Letters, 85(1), 277-288. https://doi.org/10.1016/0012-821X(87)90038-0

Christensen, N. I., & Mooney, W. D. (1995). Seismic velocity structure and composition of the continental crust: A global view. Journal of Geophysical Research: Solid Earth, 100(B6), 9761-9788.

Christeson, G. L., Goff, J. A., & Reece, R. S. (2019). Synthesis of oceanic crustal structure from two-dimensional seismic profiles. Reviews of Geophysics, 57, 504–529. https://doi.org/10.1029/2019RG000641

Cilli, P., Watts, A. B., Boston, B., & Shillington, D. J. (2023). Reprocessing of legacy seismic reflection profile data and its implications for plate flexure in the vicinity of the Hawaiian Islands. Journal of Geophysical Research: Solid Earth, 128(9), e2023JB026577. https://doi.org/10.1029/2023JB026577

Clague, D. A., Holcomb, R. T., Sinton, J. M., Detrick, R. S., & Torresan, M. E. (1990). Pliocene and Pleistocene alkalic flood basalts on the seafloor north of the Hawaiian Islands. Earth and Planetary Science Letters, 98(2), 175-191. https://doi.org/10.1016/0012-821X(90)90058-6

Conley, M. M., & Dunn, R. A. (2011). Seismic shear wave structure of the uppermost mantle beneath the Mohns Ridge, Geochemistry, Geophysics, Geosystems, 12(10). https://doi.org/10.1029/2011GC003792

Contreras-Reyes, E., Grevemeyer, I., Watts, A. B., Planert, L., Flueh, E. R., & Peirce, C. (2010). Crustal intrusion beneath the Louisville hotspot track. Earth and Planetary Science Letters, 289(3-4), 323-333. https://doi.org/10.1016/j.epsl.2009.11.020

Coombs, M. L., Clague, D. A., Moore, G. F., & Cousens, B. L. (2004). Growth and collapse of Waianae Volcano, Hawaii, as revealed by exploration of its submarine flanks. Geochemistry, Geophysics, Geosystems, 5(8). https://doi.org/10.1029/2004GC000717

Detrick, R. S., & Purdy, G. M. (1980). The crustal structure of the Kane fracture zone from seismic refraction studies. Journal of Geophysical Research: Solid Earth, 85(B7), 3759-3777. https://doi.org/10.1029/JB085iB07p03759

Detrick, R. S., White, R. S., & Purdy, G. M. (1993). Crustal structure of North Atlantic fracture zones. Reviews of Geophysics, 31(4), 439-458. https://doi.org/10.1029/93RG01952

Dunn, Robert (2024). Seismic Tomographic Model of the Hawaiian Ridge Line 02, Kaena. [Dataset]. Figshare. https://doi.org/10.6084/m9.figshare.25097543

Dunn, R. A., Lekić, V., Detrick, R. S., & Toomey, D. R. (2005). Three-dimensional seismic structure of the Mid-Atlantic Ridge (35 N): Evidence for focused melt supply and lower crustal dike injection. Journal of Geophysical Research: Solid Earth, 110(B9) https://doi.org/10.1029/2004JB003473

Dunn, RA, B MacGregor, AB Watts, C Xu, DJ Shillington (2024). Seismic Tomographic Model of the Hawaiian Ridge Line 01. [Dataset]. Figshare. https://doi.org/10.6084/m9.figshare.25097531

Flinders, A. F., Ito, G., Garcia, M. O., Sinton, J. M., Kauahikaua, J., & Taylor, B. (2013). Intrusive dike complexes, cumulate cores, and the extrusive growth of Hawaiian volcanoes. Geophysical Research Letters, 40(13), 3367-3373. https://doi.org/10.1002/grl.50633

Furumoto, A. S., & Woollard, G. P. (1965). Seismic refraction studies of the crustal structure of the Hawaiian Archipelago. Pacific Science, vol XIX, 315-319.

Furumoto, A. S., Thompson, N. J., & Woollard, G. P. (1965). The Structure of Koolau Volcano from Seismic Refraction Studies. Pacific Science, vol XIX, 306-314.

Gaherty, J. B., & Dunn, R. A. (2007). Evaluating hot spot–ridge interaction in the Atlantic from regional-scale seismic observations, Geochemistry, Geophysics, Geosystems, 8(5). https://doi.org/10.1029/2006GC001533

Gallart, J., Driad, L., Charvis, P., Sapin, M., Hirn, A., Diaz, J., et al. (1999). Perturbation to the lithosphere along the hotspot track of La Réunion from an offshore-onshore seismic transect. Journal of Geophysical Research: Solid Earth, 104(B2), 2895-2908. https://doi.org/10.1029/98JB02840

Grevemeyer, I. & Weigel, W. (1996). Seismic velocities of the uppermost igneous crust versus age. Geophysical Journal International, 124(2): 631–635.

Grevemeyer, I., Flueh, E. R., Reichert, C., Bialas, J., Kläschen, D., & Kopp, C. (2001). Crustal architecture and deep structure of the Ninetyeast Ridge hotspot trail from active-source ocean bottom seismology. Geophysical Journal International, 144(2), 414-431. https://doi.org/10.1046/j.0956-540X.2000.01334.x

Gunn, R. (1943). A quantitative study of isobaric equilibrium and gravity anomalies in the Hawaiian Islands. Journal of the Franklin Institute, 236(4), 373-390. https://doi.org/10.1016/S0016-0032(43)90275-3

Hammer, P. T. C., Dorman, L. M., Hildebrand, J. A., & Cornuelle, B. D. (1994). Jasper Seamount structure: Seafloor seismic refraction tomography. Journal of Geophysical Research: Solid Earth, 99(B4), 6731-6752. https://doi.org/10.1029/93JB02170

Hess, H. H. (1964). Seismic anisotropy of the uppermost mantle under oceans. Nature, 203(4945), 629-631. https://doi.org/10.1038/203629a0

HI-Emperor (2019). Seismic imaging of volcano construction, underplating and flexure along the Hawaiian-Emperor Seamount. [Data Set] https://ds.iris.edu/mda/18-015/

Holcomb, R. T., & Robinson, J. E. (2004). Maps of Hawaiian Islands Exclusive Economic Zone interpreted from GLORIA sidescan-sonar imagery. US Department of the Interior, US Geological Survey. https://purl.fdlp.gov/GPO/LPS56647

Hussong, D. M., Campbell, J. F., Hills, D., Peat, D., & Williams, J. (1987). Detailed mapping of the submarine geology of Oahu, Hawaii, using the SeaMARC/S system. Eos Trans. AGU, 68(44), 1336.

Leahy, G. M., Collins, J. A., Wolfe, C. J., Laske, G., & Solomon, S. C. (2010). Underplating of the Hawaiian Swell: evidence from teleseismic receiver functions. Geophysical Journal International, 183(1), 313-329. https://doi.org/10.1111/j.1365-246X.2010.04720.x

Lin, G., Shearer, P. M., Matoza, R. S., Okubo, P. G., & Amelung, F. (2014). Three-dimensional seismic velocity structure of Mauna Loa and Kilauea volcanoes in Hawaii from local seismic tomography. Journal of Geophysical Research: Solid Earth, 119(5), 4377-4392. https://doi.org/10.1002/2013JB010820

Lindwall, D. A. (1988). A two-dimensional seismic investigation of crustal structure under the Hawaiian Islands near Oahu and Kauai. Journal of Geophysical Research, 93(B10), 12107–12122. https://doi.org/10.1029/JB093iB10p12107

Lizarralde, D., Gaherty, J. B., Collins, J. A., Hirth, G., & Kim, S. D. (2004). Spreading-rate dependence of melt extraction at mid-ocean ridges from mantle seismic refraction data, Nature, 432(7018), 744-747. https://doi.org/10.1029/JB093iB04p03009.10.1038/nature03140

MacGregor, B. G., Dunn, R. A., Watts, A. B., Xu, C., & Shillington, D. J. (2023). A seismic tomography, gravity, and flexure study of the crust and upper mantle structure of the Hawaiian Ridge: 1, Journal of Geophysical Research: Solid Earth, 128(12), e2023JB027218. https://doi.org/10.1029/2023JB027218

McKenzie, D., Jackson, J., & Priestley, K. (2005). Thermal structure of oceanic and continental lithosphere. Earth and Planetary Science Letters, 233(3-4), 337-349. https://doi.org/10.1016/j.epsl.2005.02.005

Minshull, T. A., White, R. S., Mutter, J. C., Buhl, P., Detrick, R. S., Williams, C. A., & Morris, E. (1991). Crustal structure at the Blake Spur fracture zone from expanding spread profiles. Journal of Geophysical Research: Solid Earth, 96(B6), 9955-9984. https://doi.org/10.1029/91JB00431

Moore, J. G., Clague, D. A., Holcomb, R. T., Lipman, P. W., Normark, W. R., & Torresan, M. E. (1989). Prodigious submarine landslides on the Hawaiian Ridge. Journal of Geophysical Research: Solid Earth, 94(B12), 17465-17484. https://doi.org/10.1029/JB094iB12p17465

Müller, R. D., Roest, W. R., Royer, J. Y., Gahagan, L. M., & Sclater, J. G. (1997). Digital isochrons of the world's ocean floor. Journal of Geophysical Research: Solid Earth, 102(B2), 3211-3214. https://doi.org/10.1029/96JB01781

Noguchi, N., & Nakagawa, M. (2003). Geochemistry of sub-marine Southwest-O‘ahu volcano, Hawai‘i: New type of Hawaiian volcano? Geochimica et Cosmochimica Acta, 67(18), A341.

Normark, W. R., Holcomb, R. T., Searle, R. C., Somers, M. L., & Gutmacher, C. E. (1989). *Cruise report; Hawaiian GLORIA legs 3 and 4, F3-88-HW and F4-88-HW* (No. 89-213). Dept. of the Interior, US Geological Survey. https://doi.org/10.3133/ofr89213

OBSIC (2022). Ocean Bottom Seismic Instrument Center. https://obsic.whoi.edu.

Ohira, A., Kodaira, S., Moore, G. F., Yamashita, M., Fujiwara, T., Kaiho, Y., et al. (2018). Active-source seismic survey on the northeastern Hawaiian Arch: insights into crustal structure and mantle reflectors. *Earth, Planets and Space*, *70*(1), 1-16. https://doi.org/10.1186/s40623-018-0891-8

Park, J., Morgan, J. K., Zelt, C. A., & Okubo, P. G. (2009). Volcano-tectonic implications of 3-D velocity structures derived from joint active and passive source tomography of the island of Hawaii. *Journal of Geophysical Research: Solid Earth*, *114*(B9). https://doi.org/10.1029/2008JB005929

Park, J., Morgan, J. K., Zelt, C. A., Okubo, P. G., Peters, L., & Benesh, N. (2007). Comparative velocity structure of active Hawaiian volcanoes from 3-D onshore–offshore seismic tomography. *Earth and Planetary Science Letters*, *259*(3-4), 500-516. https://doi.org/10.1016/j.epsl.2007.05.008

Park, J., & Rye, D. M. (2019). Why is crustal underplating beneath many hot spot islands anisotropic? *Geochemistry, Geophysics, Geosystems*, *20*(11), 4779-4809. https://doi.org/10.1029/2019GC008492

Parsons, B., and J. G. Sclater (1977). An analysis of the variation of ocean floor bathymetry and heat flow with age. *Journal of Geophysical Research*, *82*, 803-827. https://doi.org/10.1029/JB082i005p00803

Presley, T. K., Sinton, J. M., & Pringle, M. (1997). Postshield volcanism and catastrophic mass wasting of the Waianae Volcano, Oahu, Hawaii. *Bulletin of Volcanology*, *58*(8), 597-616. https://doi.org/10.1007/s004450050165

R^{2}R (2023). Rolling Deck to Repository. [Data Set] https://www.rvdata.us/search/cruise/MGL1806.

Roland, E., Lizarralde, D., McGuire, J. J., & Collins, J. A. (2012). Seismic velocity constraints on the material properties that control earthquake behavior at the Quebrada‐Discovery‐Gofar transform faults, East Pacific Rise. *Journal of Geophysical Research: Solid Earth*, *117*(B11). https://doi.org/10.1029/2012JB009422

SAGE (2023). Seismological Facility for the Advancement of Geoscience. https://www.iris.edu/hq/

Sandwell, D. T., Harper, H., Tozer, B., & Smith, W. H. F. (2019). Gravity field recovery from geodetic altimeter missions. *Advances in Space Research*. https://doi.org/10.1016/j.asr.2019.09.011

Seton, M., Müller, R. D., Zahirovic, S., Williams, S., Wright, N. M., Cannon, J., et al. (2020). A Global Data Set of Present-Day Oceanic Crustal Age and Seafloor Spreading Parameters. *Geochemistry, Geophysics, Geosystems*, *21*(10), e2020GC009214. https://doi.org/10.1029/2020GC009214

Shor, G. G., & Pollard, D. D. (1964). Mohole site selection studies north of Maui. *Journal of Geophysical Research*, *69*(8), 1627-1637. https://doi.org/10.1029/JZ069i008p01627

Sinton, J. M., Eason, D. E., Tardona, M., Pyle, D., van der Zander, I., Guillou, H., et al. (2014). Ka‘ena Volcano—A precursor volcano of the island of O‘ahu, Hawai‘i. *GSA Bulletin*, *126*(9-10), 1219-1244. https://doi.org/10.1130/B30936.1

Strange, W. E., Woollard, G. P., & Rose, J. C. (1965a). An analysis of the gravity field over the Hawaiian Islands in terms of crustal structure. *Pacific Science*, *19*, 350-353.

Strange, W. E., Machesky, L. F., & Woollard, G. P. (1965b). A gravity survey of the island of Oahu, Hawaii. *Pacific Science*, *19*, 381-389.

Stroup, J. B., & Fox, P. J. (1981). Geologic investigations in the Cayman Trough: evidence for thin oceanic crust along the Mid-Cayman Rise. *The Journal of Geology*, *89*(4), 395-420. https://doi.org/10.1086/628605

Takahashi, E., Moore, J. G., Yokose, H., Clague, D. A., Nakagawa, M., Kani, T., et al. (2001). A newly recognized shield volcano southwest of Oahu Island, Hawaii. American Geophysical Union, Fall Meeting 2001, abstract # V12B-0981.

ten Brink, U. S., & Brocher, T. M. (1987). Multichannel seismic evidence for a subcrustal intrusive complex under Oahu and a model for Hawaiian volcanism. *Journal of Geophysical Research: Solid Earth*, *92*(B13), 13687-13707. https://doi.org/10.1029/JB092iB13p13687

ten Brink, U. S., & Brocher, T. M. (1988). Multichannel seismic evidence for variations in crustal thickness across the Molokai Fracture Zone in the Mid-Pacific. *Journal of*

Geophysical Research: Solid Earth, *93*(B2), 1119-1130. https://doi.org/10.1029/JB093iB02p01119

The MathWorks Inc. (2021). MATLAB Version: 9.11.0.1873467 (R2021b) [Software] Natick, Massachusetts: The MathWorks Inc. https://www.mathworks.com

Walcott, R. I. (1970). Flexure of the lithosphere at Hawaii. *Tectonophysics*, *9*(5), 435-446. https://doi.org/10.1016/0040-1951(70)90056-9

Walther, C. H. E. (2003). The crustal structure of the Cocos ridge off Costa Rica, *Journal of Geophysical Research: Solid Earth*, *108*(B3). https://doi.org/10.1029/2001jb000888

Watts, A. B. (1978). An analysis of isostasy in the world's oceans 1. Hawaiian-Emperor Seamount Chain. *Journal of Geophysical Research: Solid Earth*, *83*(B12), 5989-6004. https://doi.org/10.1029/JB083iB12p05989

Watts, A. B. (2001). *Isostasy and Flexure of the Lithosphere*. Cambridge University Press.

Watts, A. B., & Cochran, J. R. (1974). Gravity anomalies and flexure of the lithosphere along the Hawaiian-Emperor seamount chain. *Geophysical Journal International*, *38*(1), 119-141. https://doi.org/10.1111/j.1365-246X.1974.tb04112.x

Watts, A. B., Grevemeyer, I., Shillington, D. J., Dunn, R. A., Boston, B., & Gómez de la Peña, L. (2021). Seismic structure, gravity anomalies and flexure along the Emperor Seamount Chain. *Journal of Geophysical Research: Solid Earth*, *126*, e2020JB021109. https://doi.org/10.1029/2020JB021109

Watts, A. B., & Ribe, N. M. (1984). On geoid heights and flexure of the lithosphere at seamounts. *Journal of Geophysical Research: Solid Earth*, *89*(B13), 11152-11170. https://doi.org/10.1029/JB089iB13p11152

Watts, A. B., & ten Brink, U. S. (1989). Crustal structure, flexure, and subsidence history of the Hawaiian Islands. *Journal of Geophysical Research: Solid Earth*, *94*(B8), 10473-10500. https://doi.org/10.1029/JB094iB08p10473

Watts, A. B., ten Brink, U. S., Buhl, P., & Brocher, T. M. (1985). A multichannel seismic study of lithospheric flexure across the Hawaiian–Emperor seamount chain. *Nature*, *315*(6015), 105-111. https://doi.org/10.1038/315105a0

Watts, A. B., Tozer, B., Harper, H., Boston, B., Shillington, D. J., & Dunn, R. (2020). Evaluation of shipboard and satellite-derived bathymetry and gravity data over seamounts in the northwest Pacific Ocean. *Journal of Geophysical Research: Solid Earth*, *125*(10), e2020JB020396. https://doi.org/10.1029/2020JB020396

Watts, A. B., Zhong, S. J., & Hunter, J. (2013). The Behavior of the Lithosphere on Seismic to Geologic Timescales. *Annual Review of Earth and Planetary Sciences*, *41*(1), 443-468. https://doi.org/10.1146/annurev-earth-042711-105457

Weigel, W., & Grevemeyer, I. (1999). The Great Meteor seamount: seismic structure of a submerged intraplate volcano. *Journal of Geodynamics*, *28*(1), 27-40. https://doi.org/10.1016/S0264-3707(98)00030-1

Wessel, P. (1993). A reexamination of the flexural deformation beneath the Hawaiian Islands. *Journal of Geophysical Research: Solid Earth*, *98*(B7), 12177-12190. https://doi.org/10.1029/93JB00523

Wessel, P. (2016). Regional–residual separation of bathymetry and revised estimates of Hawaii plume flux. *Geophysical Journal International*, *204*(2), 932-947. https://doi.org/10.1093/gji/ggv472.

Wessel, P., Luis, J. F., Uieda, L., Scharroo, R., Wobbe, F., Smith, W. H. F., et al. (2019). The Generic Mapping Tools Version 6, *Geochemistry, Geophysics, Geosystems*, *20*(11), 5556-5564. https://doi.org/10.1029/2019GC008515

White, R. S., Detrick, R. S., Sinha, M. C., & Cormier, M. H. (1984). Anomalous seismic crustal structure of oceanic fracture zones. *Geophysical Journal International*, *79*(3), 779-798. https://doi.org/10.1111/j.1365-246X.1984.tb02868.x

Woollard, G. P. (1951). A gravity reconnaissance of the island of Oahu. *Eos, Transactions American Geophysical Union*, *32*(3), 358-368. https://doi.org/10.1029/TR032i003p00358

Xu, C., Dunn, R. A., Watts, A. B., Shillington, D. J., Grevemeyer, I., Gomez de la Pena, L., et al. (2022). A seismic tomography, gravity, and flexure study of the crust and upper mantle structure of the Emperor Seamounts at Jimmu guyot. *Journal of Geophysical Research: Solid Earth*, *127*(6), e2021JB023241. https://doi.org/10.1029/2021JB023241

Zucca, J. J., Hill, D. P., & Kovach, R. L. (1982). Crustal structure of Mauna Loa volcano, Hawaii, from seismic refraction and gravity data. *Bulletin of the Seismological Society of America*, *72*(5), 1535-1550. https://doi.org/10.1785/BSSA0720051535

References From the Supporting Information

Brocher, T. M. (2005). Empirical relations between elastic wavespeeds and density in the Earth's crust. *Bulletin of the seismological Society of America*, *95*(6), 2081-2092. https://doi.org/10.1785/0120050077.

Dunn, R. A., & Hernandez, O. (2009). Tracking blue whales in the eastern tropical Pacific with an ocean-bottom seismometer and hydrophone array. *The Journal of the Acoustical Society of America, 126*(3), 1084-1094. https://doi.org/10.1121/1.3158929

Dunn, R. A., Lekić, V., Detrick, R. S., & Toomey, D. R. (2005). Three-dimensional seismic structure of the Mid-Atlantic Ridge (35 N): Evidence for focused melt supply and lower crustal dike injection. *Journal of Geophysical Research: Solid Earth*, *110*(B9).

Wilkens, R. H., Firth, J., Bender, J., et al. (1993) *Proceedings of the Ocean Drilling Program, Scientific Results*, vol. 136. College Station, TX (Ocean Drilling Program).

Xu, C., Dunn, R. A., Watts, A. B., Shillington, D. J., Grevemeyer, I., Gomez de la Pena, L., et al. (2022). A seismic tomography, gravity, and flexure study of the crust and upper mantle structure of the Emperor Seamounts at Jimmu guyot. *Journal of Geophysical Research: Solid Earth*, *127*(6), e2021JB023241. https://doi.org/10.1029/2021JB023241

Tables and Figure Captions

Table 1. Comparison of Approximate Edifice Size and Flexure

	Lithospheric age at loading	Peak height of edifice above oceanic crust	Cross-sectional area of the edifice above the oceanic	Peak deflection of plate (km)	Calculated *Te* value (km)

	(Myr)	(km)	crust* (km^2)		
Ka‘ena Ridge	~82-95	7.3	800	3.5	25.6
Hawaii and Hāna	~90-95	12	1450	6-7	26.7
Jimmu Guyot	~55	8	550	3.8	14

* Not including moat fill, which also impacts the degree of flexure.

Figure 1. Free-air gravity anomaly map (Sandwell et al., 2019) of the area around the Hawaiian Islands and the seismic experiment. Heavy black lines indicate position of the seismic lines collected as part of the cruise MGL1806. The small white and gray circles indicate OBS positions. Line 02, the western line that runs approximately north-to-south is analyzed in this study. It crosses the Hawaiian Ridge at the topographic high called the Ka‘ena Ridge, and spans the Hawaiian Trough or moat (the low gravity anomaly that surrounds the ridge), and part of the Hawaiian arch. Individual strands of the Molokai Fracture Zone appear to extend beneath the island chain and intersect the seismic line. To highlight the fracture zones, the gravity contour interval is 6 mgal up to 160 mgal, thereafter it is 48 mgal - the transition roughly coinciding with the shallow water and subaerial portions of the Hawaiian Ridge.

Figure 2. Maps of the O‘ahu area showing location of the seismic line and local geographic features. Panel (a) shows locations of the OBS instruments (numbered circles) and co-located OBS and MCS seismic shot lines (heavy black line). Black dots indicate positions of the centers of ESP profiles from Watts et al. (1985). The irregular dotted curve indicates the location of the North Arch Volcanic Field. The black box indicates the area shown in (b). Panel (b) shows details of Ka‘ena Ridge and other geological features discussed in the text. The Ka‘ena Slide, Wai‘anae Slump, a large debris field, and Southwest O‘ahu Volcanic Field are labeled and their extents indicated by large-dashed lines. The dotted lines indicate the 10, 20, 30, 40, 50 mgal contours of residual Bouguer gravity (from Flinders et al., 2013). Proposed centers of volcanism for Ka‘ena and Wai‘anae volcanoes are indicated by the black and red stars, respectively. The heavy dashed lines indicate possible rift systems extending from Ka‘ena and Wai‘anae. The solid black line indicates the position of the seismic line.

Figure 3. Example of a common-receiver-gather record section for the complete seismic line (station 208, vertical geophone channel). This record highlights the *Pn* phase and its observation at distances greater than 300 km. On the north side of the instrument the *PmP* phase is faint, whereas *Pn* is strong and exhibits a weak precursor (apparent velocity ~7.7 km/s). This may be due to a stepped and more transitional nature of the crust-mantle boundary beneath the Southwest Oʻahu Volcanic Field. Within the moat area, the asymmetry of the slope of the *Pn* arrivals across the station indicates a dipping Moho (and thickening sediments) towards the Kaʻena Ridge, rather than actual differences in mantle velocity. Across the Kaʻena Ridge, the large travel time delay is probably the result of increased overall crustal thickness. Predictive deconvolution was applied to the data shown in the inset.

Figure 4. (a-f) Common-receiver-gather records (OBS shot data) for stations located across the Hawaiian moat, showing crustal and mantle phases. (g) and (h) are similar to (d) and (f), respectively, but using MCS shot data and emphasizing *P2P* arrivals using a lower reduction velocity. The station located deeper into the moat, plot (g), shows *P2P* reflections relatively delayed, as compared to the station nearer the outer edge of the moat, plot (h), indicating increased sediment thickness and down warping of the oceanic crust towards the Kaʻena Ridge. The box in (e) indicates the plot area in (i), which emphasizes the *PmP* arrival and possible sub-Moho reflection to the north of station 227 (white curve in plots (e) and (f)). A companion sub-Moho event can be seen on the south (left) side of station 231, as indicated by the white curve in (f).

Figure 5. Common-receiver-gather records for stations located across the Hawaiian Ridge. *P2P* and *PmP* phases are clearly delayed as compared with off-ridge stations. Arrows indicate *Pv* waves that passed through the center of the edifice and arrive earlier (~6.5-7.0 km/s), as compared to similar waves that travelled through the outer portions of the edifice (~5.0-5.5 km/s). (e) shows an additional arrival from the interior of the landslide portion of the edifice. (f) Shows one of the possible sub-Moho arrivals that are observed intermittently along the seismic line.

Figure 6. Travel times of the seismic phases used for tomographic imaging, color-coded by seismic phase. Station numbers and their positions are indicated by the labels. To better show the coherency of the seismic phases from station to station, the range to each pick has been divided

by two before plotting. This is effective because the slope of each travel time curve is dependent on the wave speed at the turning depth of the ray, which is approximately halfway between the shot and station.

Figure 7. Travel times of the *Pn* seismic phase using a reduced time axis to align the arrival times. (a) Shows all *Pn* travel time data; no single reduction velocity satisfies all regions of the data. In particular, rays that undershoot the ridge are greatly misaligned at this reduction velocity. (b) Shows data with ranges >100 km that undershoot the ridge axis recorded by off-axis stations (stations 203-212, 224-235) and off-axis shots, for two different reduction velocities. A velocity of 8.25 km/s (green values) provides an overall good alignment, despite local structural variations. A value of 7.8 km/s (gray values), provides poor alignment. (c) Shows data with ranges <100 km (omits ridge undershoot paths), and reveals an improvement in alignment over data shown in (a) for most areas away from the ridge (green dots) using a lower reduction velocity. As in Fig. 6, the range of each pick is divided by two.

Figure 8. Final *P*-wave tomographic image (mean of all models), along with both the shallow reflector (upper red curve), whose position is controlled by the *P2P* phase and deeper refractions, and the deeper reflector (lower red curve), whose position is controlled by the *PmP* and *Pn* phases. The vertical exaggeration is a factor of 8.

Figure 9. Comparison of the calculated gravity effect of the tomographic image with the observed free-air gravity anomaly. a) Observed and calculated free-air gravity anomaly. The observed gravity is based on the 1 s converted BGM-3 count data with a 120 s Gaussian filter (gray filled circles) and an additional 1.0 km median filter (red solid line). The calculated gravity is based on the tomographic image in Figure 8, the Nafe-Drake and Christensen and Mooney empirical relationships between *P* wave velocity and density (solid black line) and a continuous 3D elastic plate (flexure) model based on a load density of 2737 kg/m^3, an average infill density of 2450 kg/m^3, an elastic thickness, T_e, of 25.6 km, and an assumed thickness of the pre-flexed oceanic crust of 6.04 km (dashed orange line). Light blue profile shows the calculated gravity effect of the bathymetry based on a 2D (solid line) and 3D (dashed line) model. b) *P* wave velocity contours (in km/s) and densities (in kg/m^3) used in the calculation of the gravity anomalies. The light blue shaded area shows the calculated flexure of the oceanic crust based on the same parameters as used in the gravity calculation.

Figure 10: Schematic model showing an interpretation of the seismic image. Melts rising through the cold lithosphere react with the host rock leaving behind higher density and wave speed minerals, such as olivine. As the melts move into the edifice, they enter a large mush zone that increases in elevation as the volcano grows. A small neighboring locus of melt injection is also observed on the south side of the main volcanic core. Some “off-ridge” melts may rise up to form the Southwest Oʻahu Volcanic field, the North Arch volcanics, and occasional mantle-level melt sills.

Figure 1.

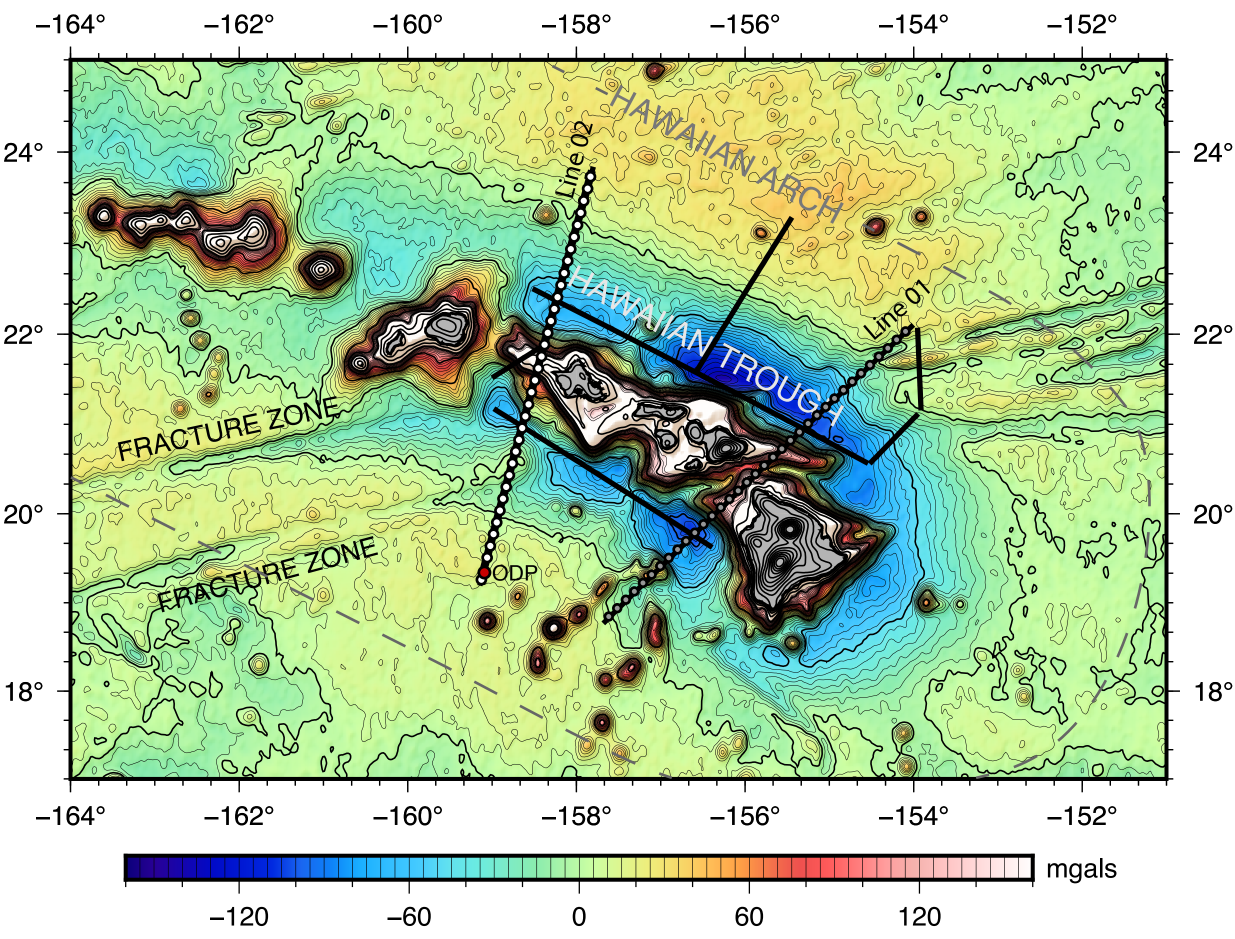

−164°
−162°
−160°
−158°
−156°
−154°
−152°
24°
22°
20°
18°
HAWAIIAN ARCH
HAWAIIAN TROUGH
Line 02
Line 01
FRACTURE ZONE
FRACTURE ZONE
ODP
mgals
−120
−60
0
60
120

Figure 2.

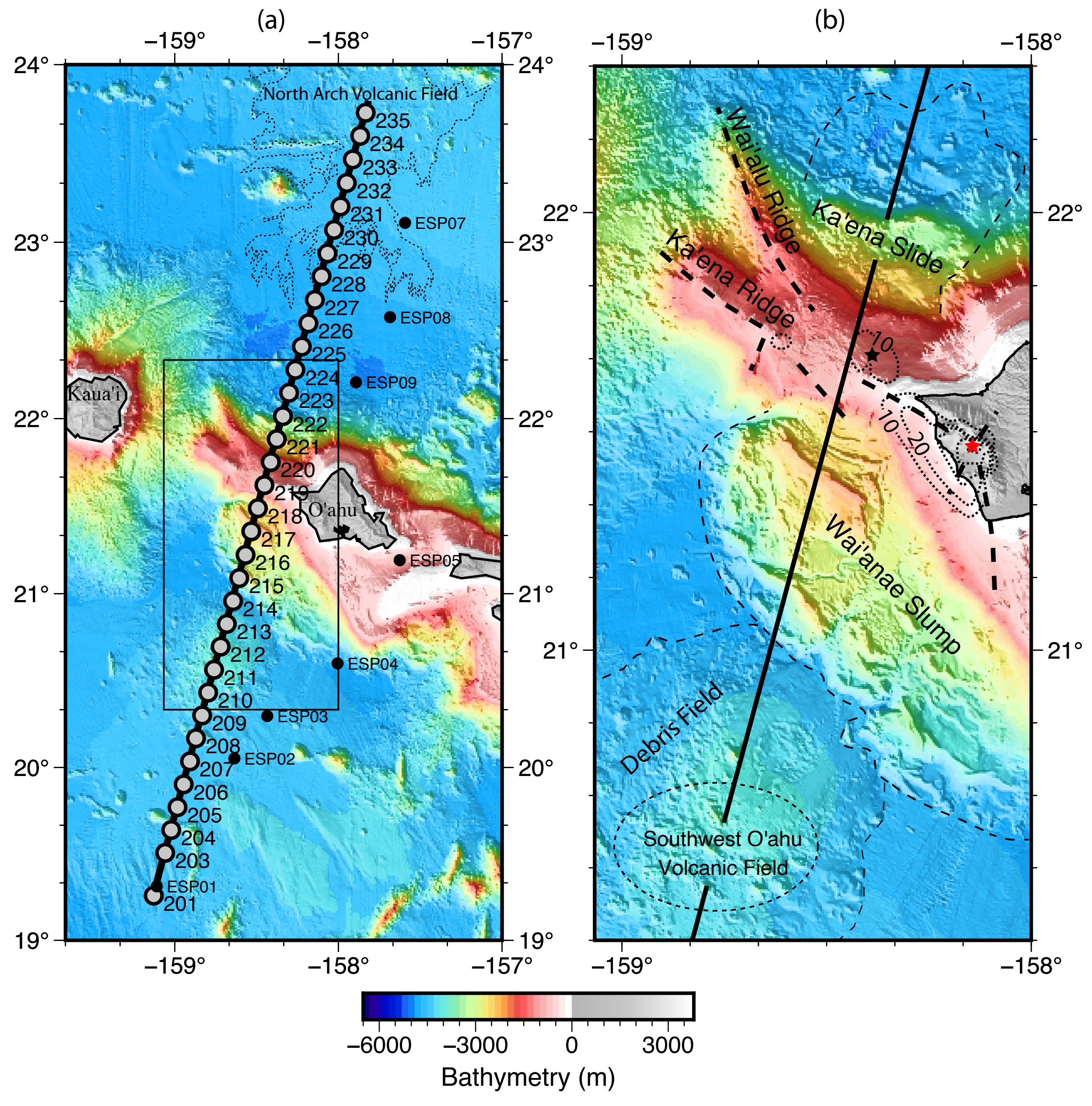

(a)
(b)
North Arch Volcanic Field
Kaua'i
O'ahu
ESP01
ESP02
ESP03
ESP04
ESP05
ESP07
ESP08
ESP09
201
203
204
205
206
207
208
209
210
211
212
213
214
215
216
217
218
219
220
221
222
223
224
225
226
227
228
229
230
231
232
233
234
235
Wai'alu Ridge
Ka'ena Ridge
Ka'ena Slide
Wai'anae Slump
Debris Field
Southwest O'ahu Volcanic Field
10
20
−159°
−158°
−157°
24°
23°
22°
21°
20°
19°
−6000
−3000
0
3000
Bathymetry (m)

Figure 3.

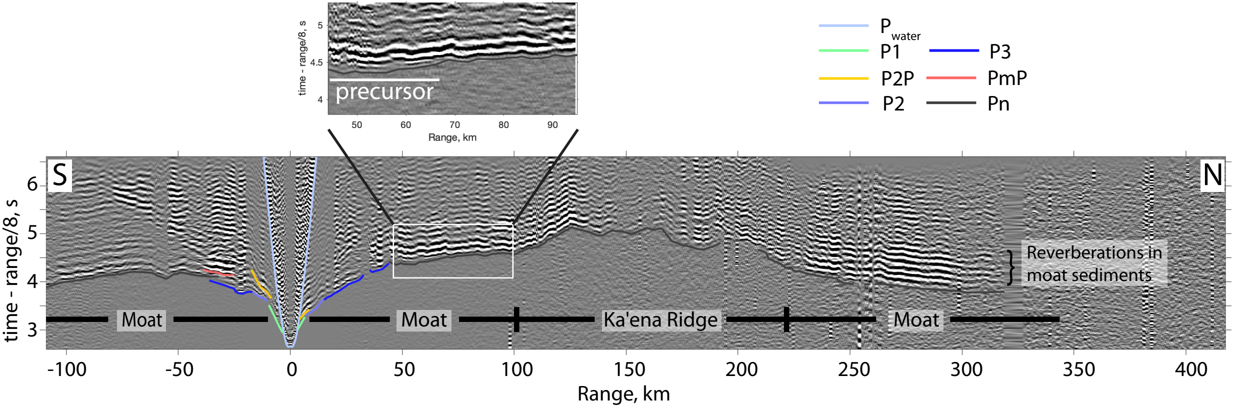

time - range/8, s
5
4.5
4
precursor
50
60
70
80
90
Range, km
P water
P1
P2P
P2
P3
PmP
Pn
S
N
6
5
4
3
time - range/8, s
Reverberations in
moat sediments
Moat
Moat
Ka'ena Ridge
Moat
-100
-50
0
50
100
150
200
250
300
350
400
Range, km

Figure 4.

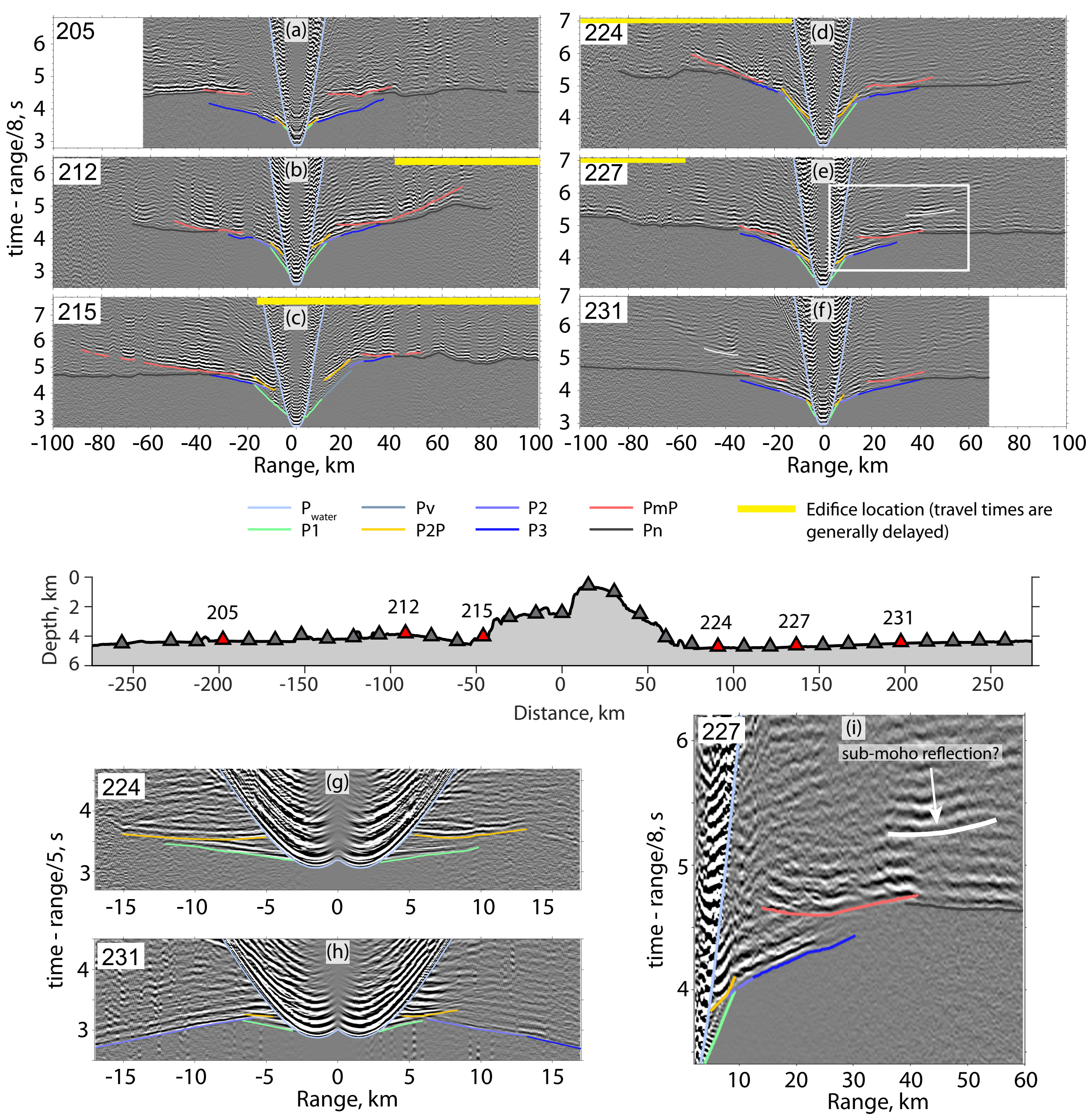

205
(a)
212
(b)
215
(c)
224
(d)
227
(e)
231
(f)
time - range/8, s
Range, km
P water
P1
Pv
P2P
P2
P3
PmP
Pn
Edifice location (travel times are generally delayed)
Depth, km
Distance, km
224
(g)
231
(h)
time - range/5, s
Range, km
227
(i)
sub-moho reflection?
time - range/8, s
Range, km

Figure 5.

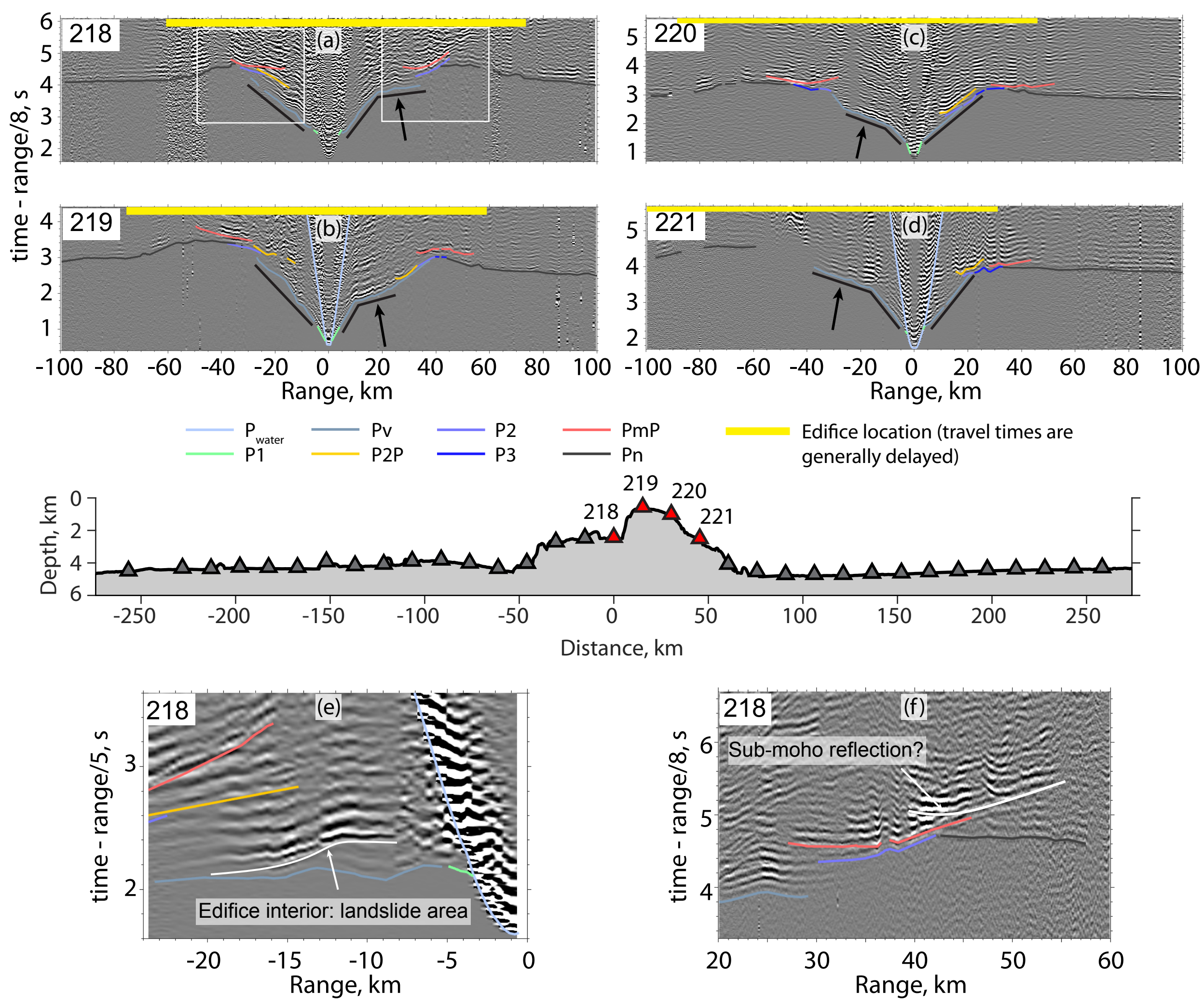

218
(a)
219
(b)
220
(c)
221
(d)
time - range/8, s
Range, km
P water
P1
Pv
P2P
P2
P3
PmP
Pn
Edifice location (travel times are generally delayed)
Depth, km
Distance, km
218
219
220
221
218
(e)
Edifice interior: landslide area
time - range/5, s
Range, km
218
(f)
Sub-moho reflection?
time - range/8, s
Range, km

Figure 6.

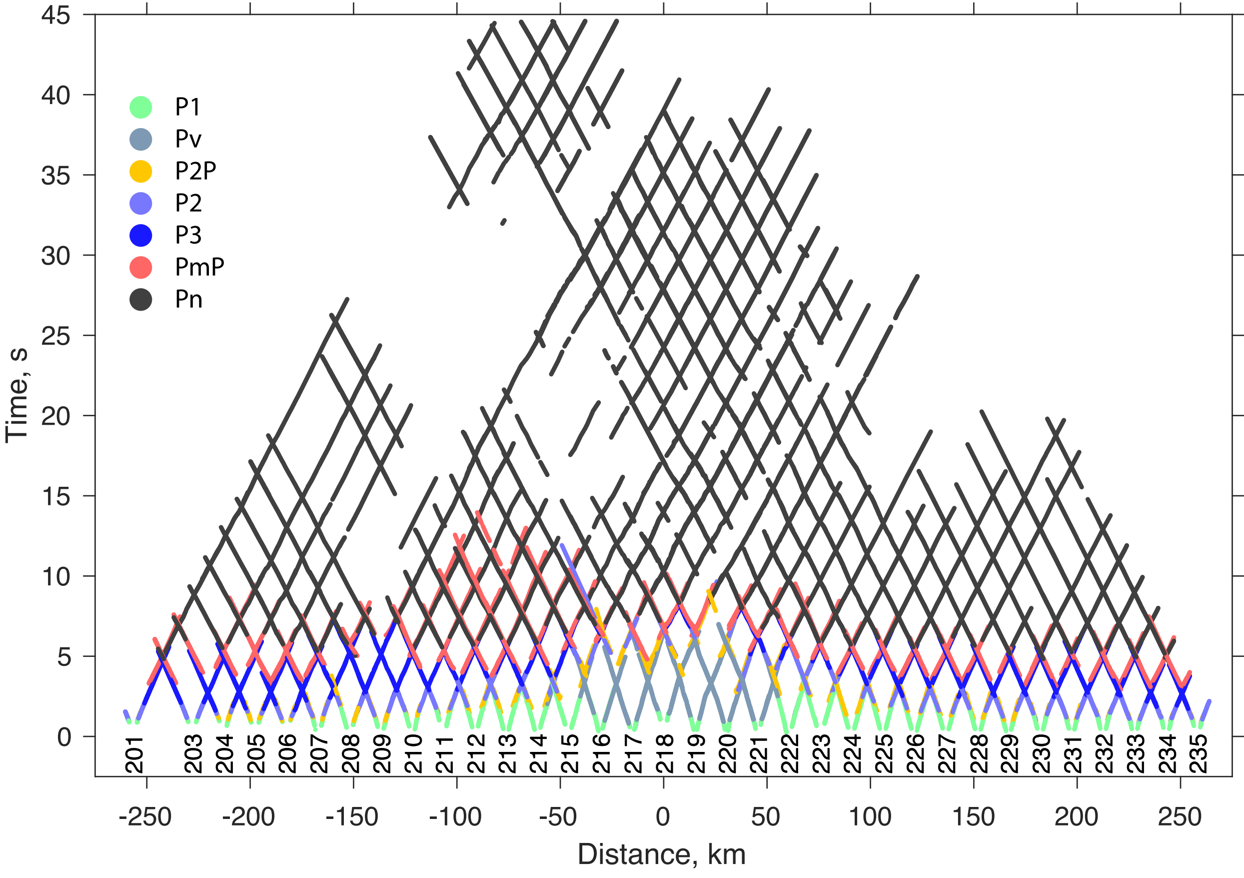
Time, s
Distance, km
P1
Pv
P2P
P2
P3
PmP
Pn
201
203
204
205
206
207
208
209
210
211
212
213
214
215
216
217
218
219
220
221
222
223
224
225
226
227
228
229
230
231
232
233
234
235

Figure 7.

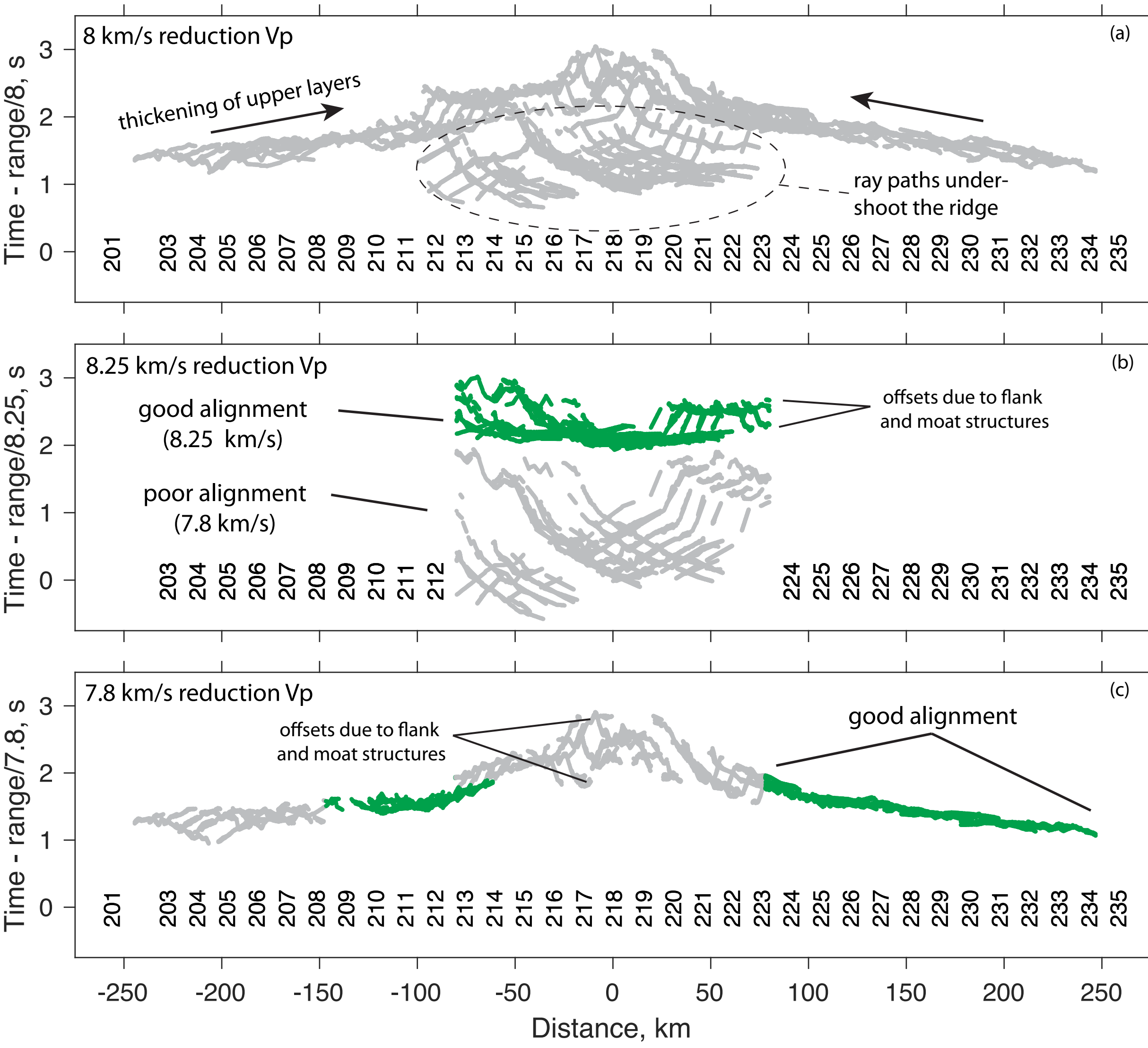
8 km/s reduction Vp
(a)
thickening of upper layers
ray paths under-shoot the ridge
8.25 km/s reduction Vp
(b)
good alignment (8.25 km/s)
poor alignment (7.8 km/s)
offsets due to flank and moat structures
7.8 km/s reduction Vp
(c)
offsets due to flank and moat structures
good alignment
Time - range/8, s
Time - range/8.25, s
Time - range/7.8, s
Distance, km

Figure 8.

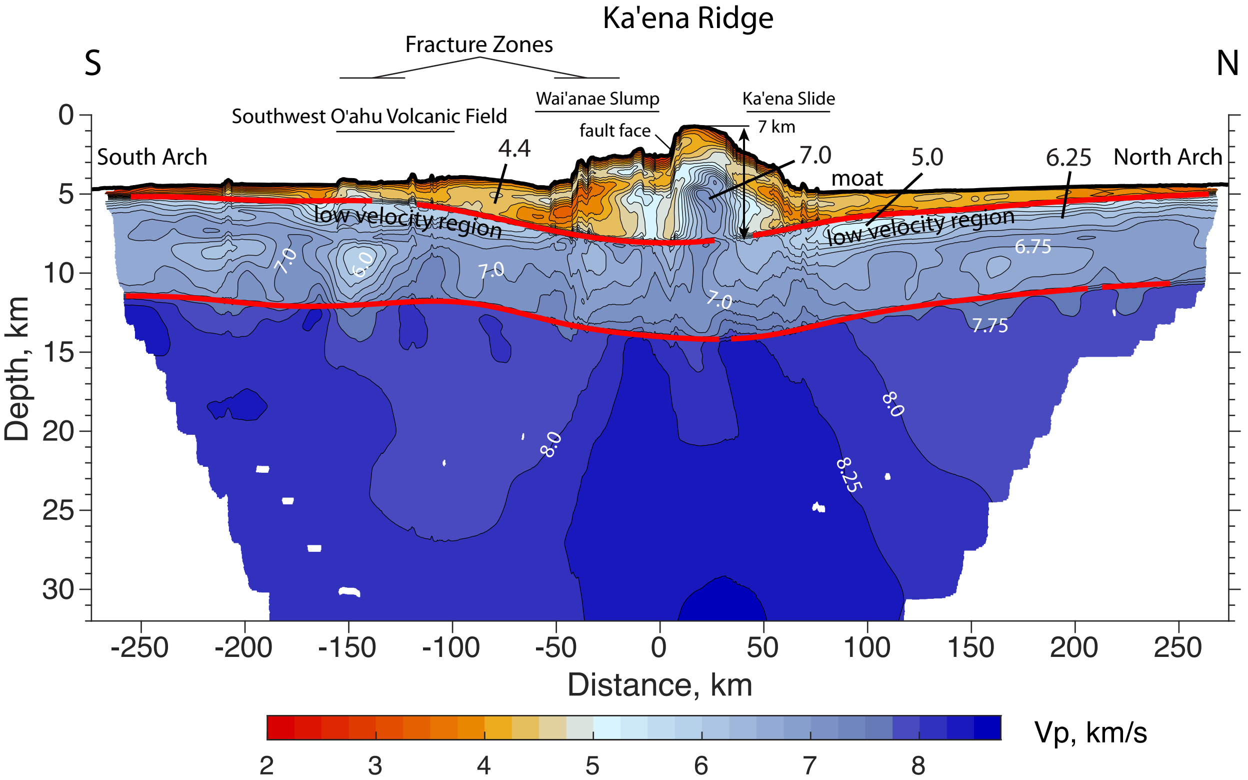
Ka'ena Ridge
Fracture Zones
S
N
Wai'anae Slump
Ka'ena Slide
Southwest O'ahu Volcanic Field
fault face
7 km
South Arch
4.4
7.0
5.0
6.25
North Arch
moat
low velocity region
low velocity region
7.0
6.0
7.0
7.0
6.75
7.75
8.0
8.0
8.25
Depth, km
0
5
10
15
20
25
30
-250
-200
-150
-100
-50
0
50
100
150
200
250
Distance, km
2
3
4
5
6
7
8
Vp, km/s

Figure 9.

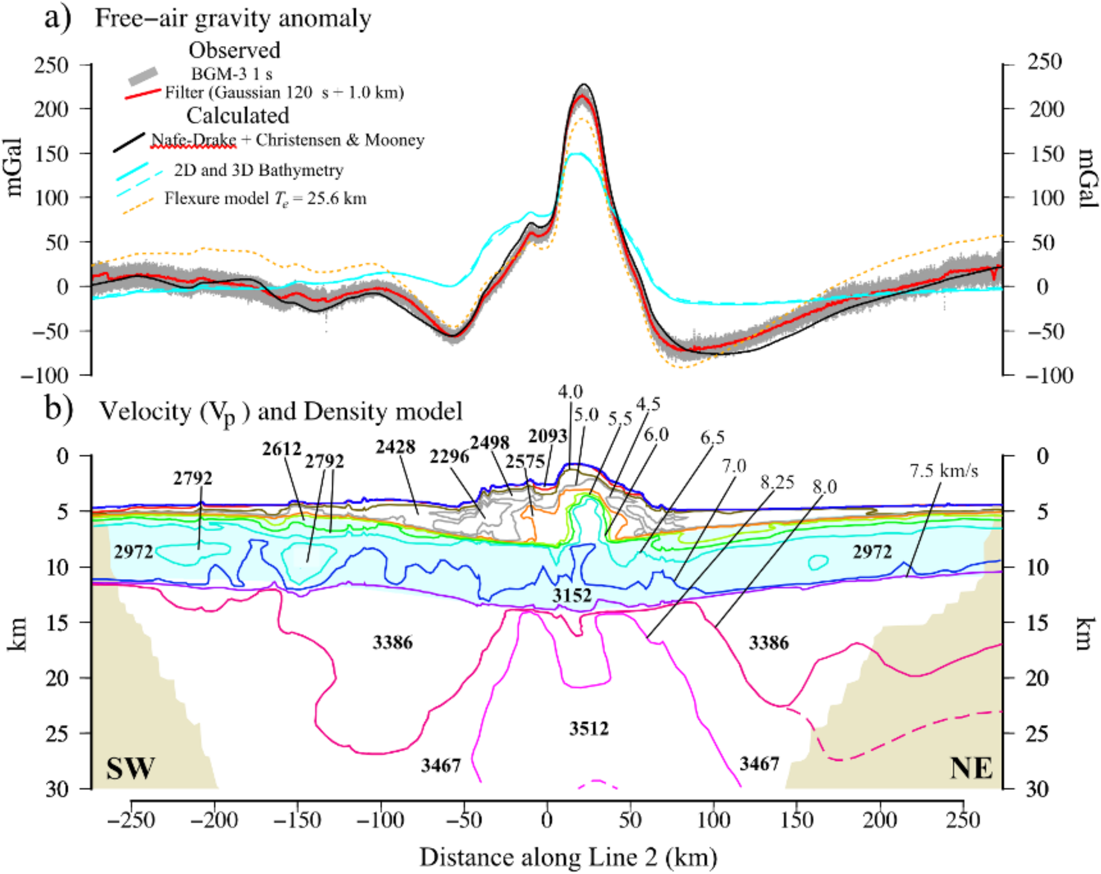
a) Free−air gravity anomaly
Observed
BGM-3 1 s
Filter (Gaussian 120 s + 1.0 km)
Calculated
Nafe-Drake + Christensen & Mooney
2D and 3D Bathymetry
Flexure model T_e = 25.6 km
mGal
b) Velocity (V_p) and Density model
4.0
5.0
5.5
4.5
6.0
6.5
7.0
8.25
8.0
7.5 km/s
2792
2612
2792
2428
2296
2498
2575
2093
2972
2972
3152
3386
3386
3512
3467
3467
SW
NE
km
Distance along Line 2 (km)

Figure 10.

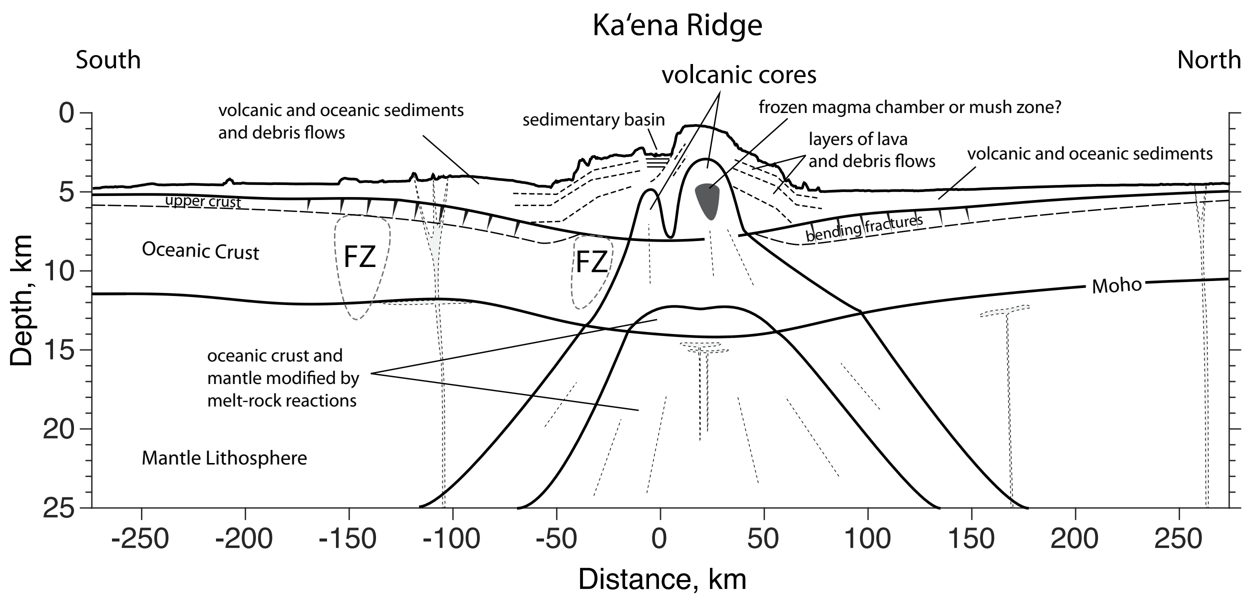
Ka'ena Ridge
South
North
volcanic cores
volcanic and oceanic sediments
and debris flows
sedimentary basin
frozen magma chamber or mush zone?
layers of lava
and debris flows
volcanic and oceanic sediments
upper crust
bending fractures
Oceanic Crust
FZ
FZ
Moho
oceanic crust and
mantle modified by
melt-rock reactions
Mantle Lithosphere
Depth, km
0
5
10
15
20
25
-250
-200
-150
-100
-50
0
50
100
150
200
250
Distance, km